NEUROSCIENCE

Predictive neural computations in the cerebellum contribute to motor planning and faster behavioral responses in larval zebrafish

Sriram Narayanan, Aalok Varma, Vatsala Thirumalai*

The ability to predict the future based on past experience lies at the core of the brain's ability to adapt behavior. However, the neural mechanisms that participate in generating and updating predictions are not clearly understood. Further, the evolutionary antecedents and the prevalence of predictive processing among vertebrates are even less explored. Here, we show evidence of predictive processing via the involvement of cerebellar circuits in larval zebrafish. We presented stereotyped optic flow stimuli to larval zebrafish to evoke swims and discovered that lesioning the cerebellum abolished prediction-dependent modulation of swim latency. When expectations of optic flow direction did not match with reality, error signals arrive at Purkinje cells via the olivary climbing fibers, whereas granule cells and Purkinje cells encode signals of expectation. Strong neural representations of expectation correlate with faster swim responses and vice versa. In sum, our results show evidence for predictive processing in nonmammalian vertebrates with the involvement of cerebellum, an evolutionarily conserved brain structure.

INTRODUCTION

Predictive processing theory holds that the brain is able to generate predictive models based on incoming sensory input, use such predictions to adapt behavior, and constantly update these models by calculating prediction errors (*1*, *2*). Such models predict the consequences of motor commands (*3*–*5*), expected rewards (*6*), or the future states of sensory variables (*7*–*9*). These actions allow animals to respond faster, enhance reward, or avoid dangerous or undesirable situations. Nevertheless, the neural mechanisms underlying generation and use of predictive models are not clearly understood. Specifically, the mechanisms underlying the generation of predictions, error signals, and the accumulation of new evidence are relatively unknown in the context of ethologically relevant behaviors. Further, although the centrality of predictive processing to aspects of brain function ranging from sensorimotor control to planning and decision-making is much appreciated, its prevalence outside of mammalian nervous systems is not well-documented.

Previous studies in mammals have identified neural signals associated with predictive processing in the neocortex (*7*, *10*, *11*), cerebellum (*12*, *13*), and the dopaminergic reward system (*14*). In particular, the cerebellum is thought to control movements by acquiring predictive models of the motor system and the environment (*15*, *16*). Recently, the predictive functions of the cerebellum have been shown to be more generally applicable to nonmotor domains, such as in encoding the expectation of rewards (*17*–*19*). The cerebellum is also one of the oldest parts of the vertebrate brain, with cell types and connectivity well conserved in all vertebrates from fish to mammals (*20*, *21*). Here, we establish the larval zebrafish experimental system, taking advantage of its tractability, to study how the cerebellum uses error feedback to acquire predictive models of the environment over behaviorally relevant timescales. We show that larval zebrafish use cerebellar circuits to acquire and update predictions of perception by integrating sensory evidence over minute timescales and such predictions drive swimming decisions.

In larval zebrafish, the cerebellum is functional by 5 days postfertilization (dpf) concomitant with the emergence of motor behaviors (*22*). At these stages, its small size and transparency allow the imaging of a substantial proportion of all cells in the cerebellum. Previous studies have shown that the larval zebrafish cerebellum is involved in associative learning (*23*) as seen in other species and that cerebellar neurons are activated before swim bouts, suggesting a role in motor planning (*24*).

Larval zebrafish sense optic flow and generate compensatory swims in the same direction [optomotor response (OMR)] (*25*–*27*). The OMR is believed to help them stabilize their position in flowing water and can be reliably evoked in head-restrained fish by providing optic flow stimuli in the caudo-rostral direction on a screen placed beneath them (*28*). Earlier studies have investigated OMR from a sensorimotor point of view. These studies show that the decision to swim is driven by a leaky integration of visual input (*29*) and that the latency to initiate swims depends strongly on the optic flow velocity (*30*, *31*). However, whether prior experience induces predictive modulation of OMR has not yet been investigated. Here, we sought to ask whether larvae can learn an expectation of OMR stimulus pattern and use such information to modulate their swim output.

In this study, we conducted a series of experiments on head-restrained larval zebrafish in a closed-loop optomotor environment while simultaneously imaging calcium activity of specific cell types in the cerebellum. We first acclimatized larvae to repetitive forward-going optic flow pulses and then showed a deviant stimulus in a different direction. Our results indicate a causal role for the cerebellar circuit and directionally tuned Purkinje cells (PCs) particularly in signaling deviation from an expected pattern and in planning the motor response. We find that through this mechanism, larval zebrafish acquire predictions of their sensory world from experience, update these predictions when deviations occur, and adjust their motor behavior accordingly.

National Centre for Biological Sciences, Tata Institute of Fundamental Research, Bangalore 560065, India.
*Corresponding author. Email: vatsala@ncbs.res.in

RESULTS

Unexpected stimuli cause a cerebellum-dependent transient elevation in swim latency

We presented repetitive forward-going optic flow pulses with closed-loop feedback to head-restrained larval zebrafish to test whether they can learn stimulus patterns from experience. Closed-loop feedback was used to keep fish engaged with the stimulus as they go into a passive, unresponsive state in the open-loop condition (*32*). In 10% trials, we pseudo-randomly interspersed the repetitive forward flow pulses (1 cm/s) with "probe" stimuli. Probe stimuli were optic flow pulses of the same duration as the forward-going stimuli but in the backward direction and much lower velocity (0.064 cm/s). Probe stimuli seldom triggered any motor bouts (Fig. 1, A, B, and F).

In head-restrained larval zebrafish, the latency to generate swim response depends on multiple parameters such as the flow velocity and the sensorimotor feedback (*28*, *30*, *31*). Further, in experiments where sensorimotor feedback was changed suddenly,

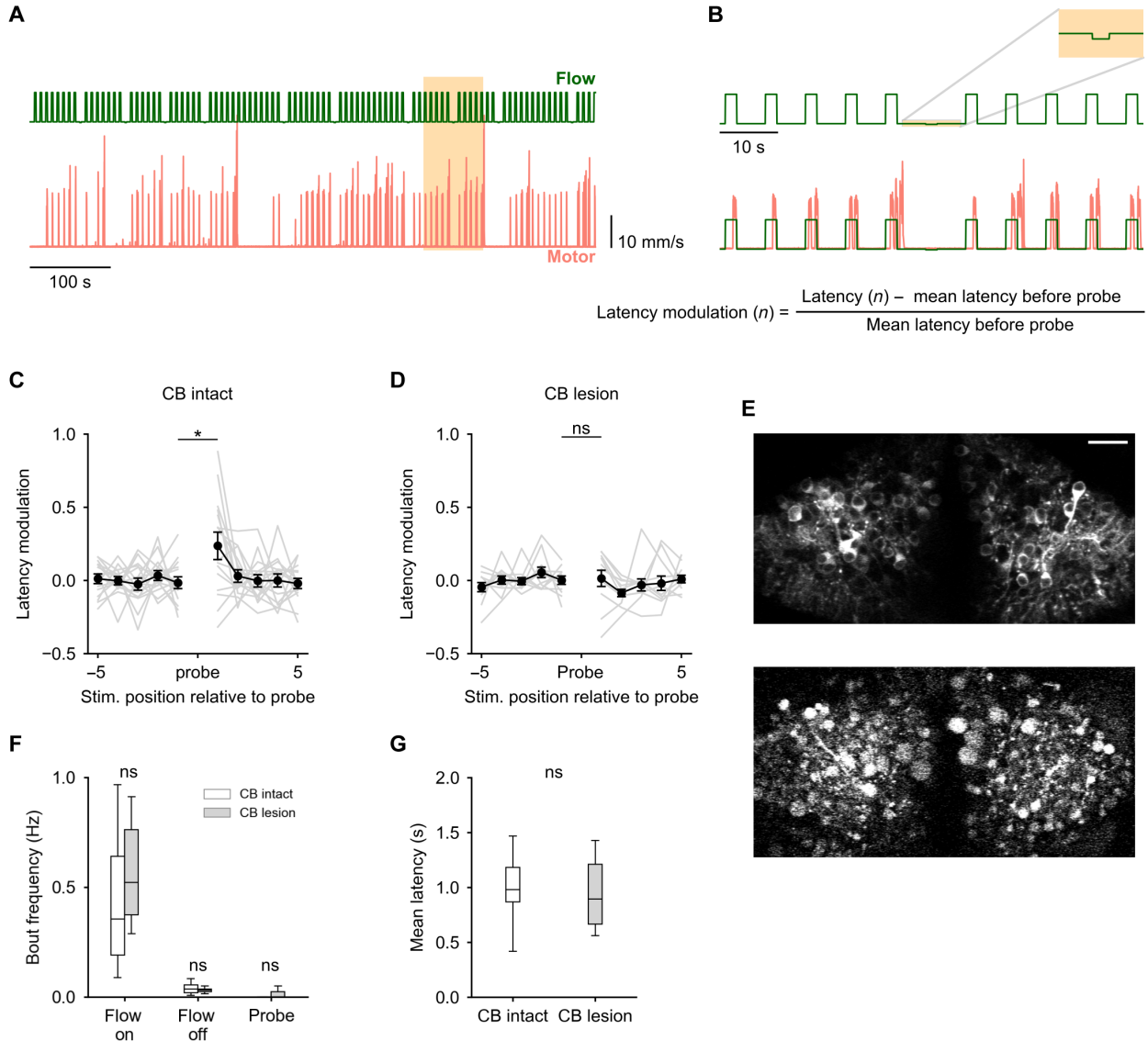

Fig. 1. The cerebellum uses a learnt expectation of optic flow stimulus to generate swims with lower latency. (**A**) Optic flow stimulus protocol used (green) and corresponding motor responses of a representative fish (pink). The positions of the probe stimuli were randomized. (**B**) Zoomed-in view of the highlighted region in (A) Top: A probe stimulus ±5 forward optic flow pulses. Bottom: Calculation of latency modulation around the probe. (**C**) Average latency modulation for 10 forward optic flow pulses around the probe stimulus. $N = 17$ fish. Unexpected probe stimuli cause a transient elevation in latency. (**D**) Latency modulation around the probe stimulus for cerebellum (CB) lesioned fish. $N = 11$. Probe stimuli did not cause an elevation in latency in lesioned fish. (C) and (D) $^*P = 0.013$; nonsignificant (ns), $P > 0.05$ by linear mixed-effects evaluating pre-probe versus post-probe latency modulation with an interaction effect of lesion. (**E**) A single two-photon optical section of the GCaMP6s expressing PCs before (top) and after (bottom) lesioning. Disintegration and blebbing of cells and neuropil can be seen after the lesioning protocol. Scale bar, 20 μm. (**F** and **G**) Both lesioned and nonlesioned fish show similar levels of behavioral responsiveness (F) and respond to optic flow with similar average latency (G). ns, $P > 0.05$ by independent sample *t* test.

latency changed on a much slower timescale compared to other bout parameters (*28*). On the basis of this, we reasoned that swim latency may be influenced by predictions of stimulus patterns and likely to reflect longer timescale computations within the network. Occurrence of probe stimuli, which would trigger a mismatch between a prediction and sensory input, will then be expected to modulate swim bout latency in trials immediately following them. To quantify this, we looked at a window of five optic flow stimulus pulses before and after a probe stimulus (Fig. 1, A and B). The average latency in the window before the probe was considered as the baseline and a fold change in latency from this baseline was calculated for each of the 10 stimulus pulses in the window around the probe (Fig. 1B). The probe stimulus caused a significant elevation in latency in response to the next occurrence of the forward optic flow stimulus. The elevated latency returned to baseline after a single pulse of the forward optic flow stimulus following the probe (Fig. 1C). This suggests that fish use expectations based on stimulus history to generate OMRs.

To test a causal role for the cerebellum in this process, we lesioned the cerebellum (Fig. 1E) in a different group of fish and performed the same experiment as above. Both lesioned and non-lesioned fish showed similar levels of behavioral responsiveness, and the mean latency remained comparable between both groups (Fig. 1, F and G). However, the lesioned fish did not show an elevation in latency after the probe stimulus was presented (Fig. 1D). The fact that behavior was not perturbed by an unexpected stimulus in lesioned fish indicates that the cerebellum is involved in incorporating expectations based on stimulus history in the generation of swim responses to optic flow, possibly with lower latency.

PCs exhibit direction-tuned responses to optic flow

We next proceeded to analyze the circuits in the cerebellum that might encode for stimulus history–dependent predictions and errors. In fish and mammals, PCs are the principal neurons in the cerebellum that integrate sensory and motor information from disparate brain areas. To record PC population activity during our behavioral task, we used calcium imaging in head-restrained larval zebrafish (see Materials and Methods). PCs receive excitatory inputs from granule cells (GCs) via parallel fibers (PF) and strong excitation from the inferior olive (IO) via climbing fibers (CFs). PFs, via the modulation of simple spiking and CFs, by triggering calcium influx into PC dendrites, contribute to transient peaks in dF/F signals in PCs (*33*–*35*). CFs are tuned for specific optic flow directions (*36*) implying that PCs might also show directional tuning when forward or backward optic flow stimuli are presented.

To characterize the directional response properties of PCs to optic flow stimuli, we recorded calcium activity in head-restrained larval zebrafish swimming in a one-dimensional (1D) closed-loop optomotor environment using two-photon microscopy (Fig. 2, A and B). Fish were initially presented with randomly interspersed pulses of 2-s duration, of forward (+ve)– or backward (−ve)–moving gratings at 1 cm/s or a probe stimulus, where the gratings moved 0.064 cm/s in the forward (+ve probe) or backward (−ve probe) direction (Fig. 2C). Each stimulus was presented five times per fish with an interval of 5 s between them (Fig. 2C). We then fit the calcium responses of individual cells using forward, backward, and motor regressors using multiple linear regression and selected cells whose responses could be fit with a coefficient of determination (R^2) ≥ 0.6 (Fig. 2D) (*35*, *37*). When we grouped cells on the basis of the largest regression coefficient, we found that they segregated into either "forward"- or "backward"-tuned (fig. S1A), and there were no cells that were strongly activated by both directions of optic flow (fig. S1, A and D). Fewer cells were found to be active during motor events compared to the number of cells that were activated by optic flow. The motor-correlated cells were also typically activated when forward optic flow stimuli were presented (Fig. 2E, row 4, column 1). This could be because of two reasons: Because forward optic flow stimuli reliably evoked swims, PCs involved in generating the OMR could be activated by both sensory input as well as motor activity; or, the strong correlation between motor activity and the forward optic flow stimulus could make it difficult to distinguish between them using regression. When we segregated the stimulus pulses based on the presence or absence of motor activity, we found that motor-correlated cells did not show a peak in calcium activity to flow stimuli alone, indicating that their responses were specific to the presence of motor activity (Fig. 2E, solid line, row 4, column 1).

We then proceeded to classify cells as either forward, backward, or "motor" based on the largest regression coefficient and strong correlation [Pearson's correlation coefficient (r) ≥ 0.6] with the respective regressor. Using this approach, we were able to classify 24 ± 12% (means ± SD) of all cells in one of the three groups. This classification was used in subsequent trials to group cells based on their tuning. Optic flow stimuli in both the forward (+ve) and backward (−ve) directions at 1 cm/s caused strong activation in distinct populations of PCs (Fig. 2E, columns 1 and 3). These forward and backward PCs responded preferentially to the positive and negative probe stimuli, respectively. However, both the positive and negative probe stimuli, being 15 times weaker than the optic flow stimuli at 1 cm/s, caused a much lower but detectable activation in PCs of the respective directional tuning (Fig. 2E, columns 2 and 4). PC responses measured using this random stimulus sequence were considered as baseline for comparisons in the subsequent experiments. Forward-moving gratings at 1 cm/s reliably evoked swims. As before, there were rarely any swims in response to the probe stimuli (Fig. 2D). Backward-moving gratings at 1 cm/s either failed to induce swim responses or caused struggles and/or large-amplitude turns and hence were not presented subsequently.

Response to optic flow in PCs is modulated by stimulus history

After the first trial where stimuli were presented in random order (Figs. 2C and 3A), subsequent trials in the next phase of the experiment were conducted to test whether stimulus history influences PC response to deviant optic flow stimuli. We acclimatized fish with eight repetitions of 2-s-long forward optic flow stimuli at 1 cm/s, which consistently evoked slow forward swims in closed loop (Fig. 3, B to E). The trials then proceeded into a probe phase where different probe stimuli were presented as shown in Fig. 3A. These stimuli were either three pulses of the negative probe stimulus, three pulses of the positive probe stimulus, or stationary gratings (no probe). In addition to these trials, a fourth trial was included where acclimatization pulses were presented at randomized time intervals (range, 1.5 to 8.5 s; mean, 5 s) instead of the fixed 5-s interval, followed by three pulses of the negative probe stimulus. Each of the trials was presented three times in a different randomized order for every fish, and the responses were averaged by trial type for each cell. We then analyzed the effect of acclimatization on the response to probe stimuli, with respect to baseline responses measured when stimuli were presented in random order in the first trial.

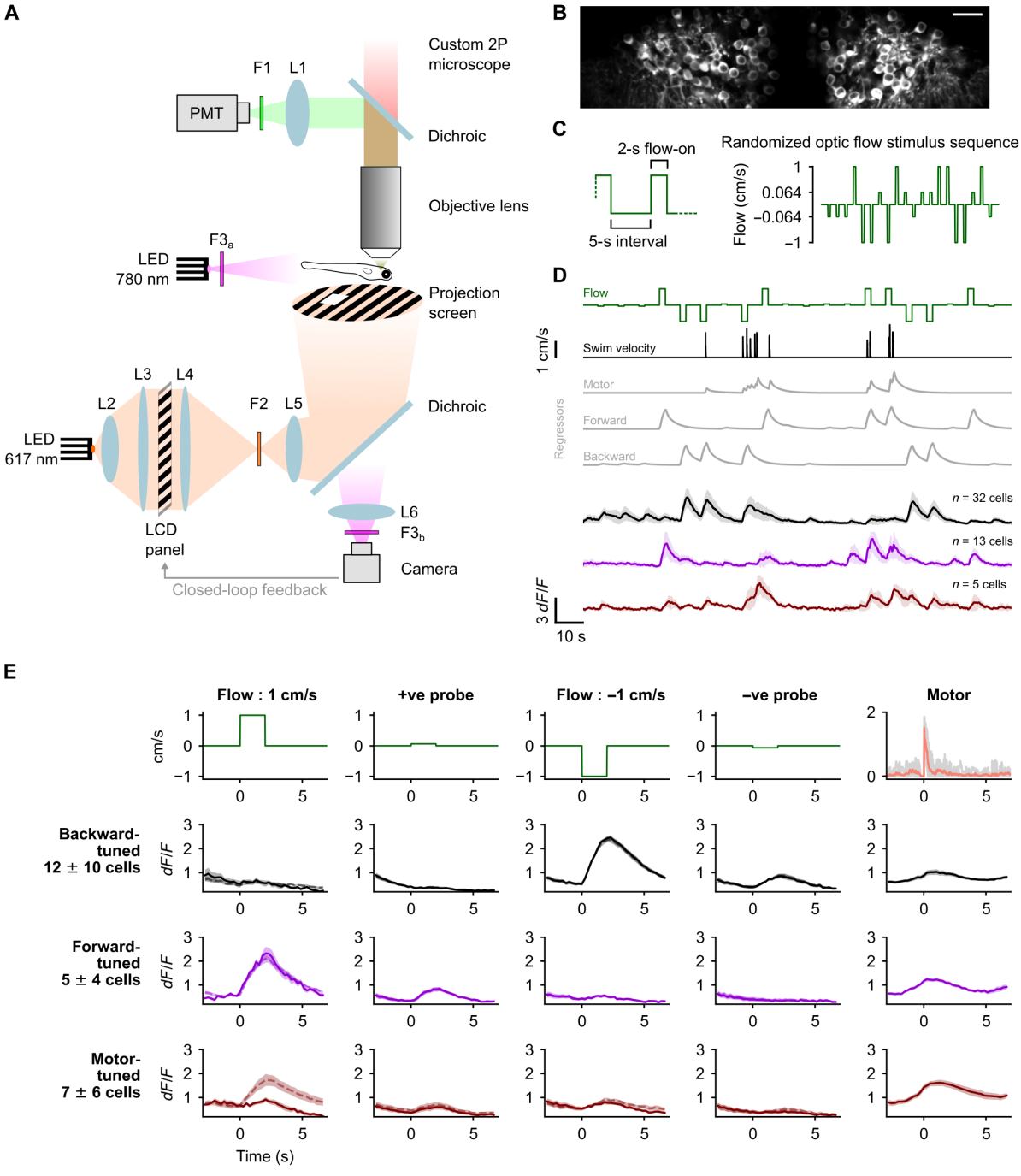

Fig. 2. Purkinje cells (PCs) show direction selective responses to optic flow stimuli. (**A**) Schematic of the experimental setup. (**B**) Average two-photon image of PCs expressing GCaMP6s from a representative fish. Scale bar, 20 μm (**C**) Left: Zoomed-in view of the stimulus protocol highlighting the 5-s interval between two stimulus pulses and the 2-s pulse duration. Right: An example of the randomly ordered optic flow stimulus presented in the first trial. Note: The *y* axis is scaled nonlinearly in this schematic to highlight the small-amplitude probe stimuli. (**D**) Classification of PCs based on tuning as backward (black), forward (magenta), or motor (brown) using regressors (gray) in a representative fish, shown as means ± SD. (**E**) Average response profiles across fish of backward-, forward-, and motor-tuned cells (rows 2, 3, and 4, respectively) aligned to the start of each stimulus (columns 1 to 4) or motor activity (column 5); shaded regions around the average calcium traces are SEM over $N = 8$ fish. The first row shows the respective optic flow stimulus (columns 1 to 4) and average motor activity (column 5). Solid lines in columns 1 to 4 are average responses for stimulus presentations without motor activity, and the dashed lines are averages for all presentations including those with motor activity. Motor activity traces in gray represent the average for individual fish.

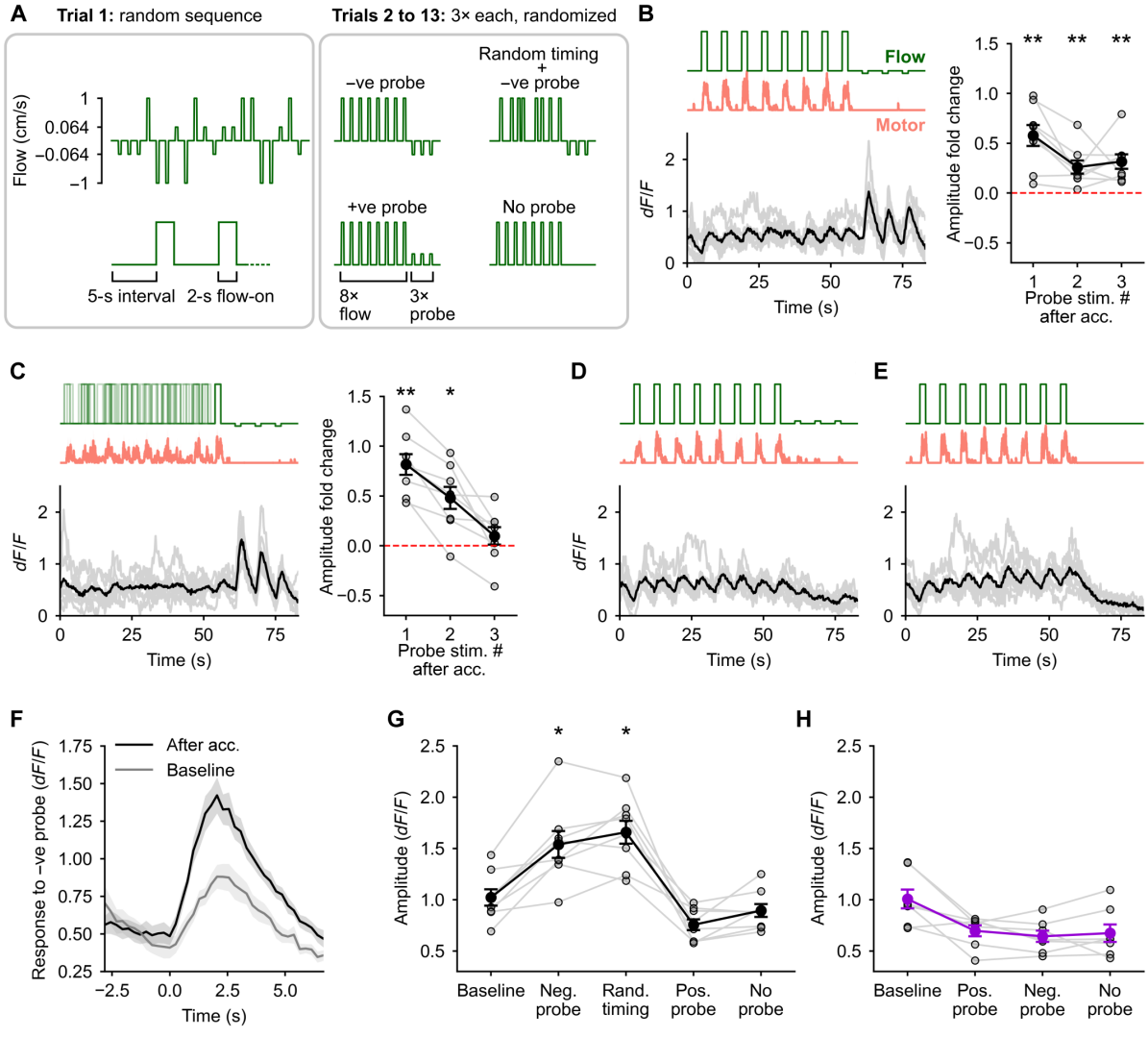

Fig. 3. A change in optic flow direction is encoded in enhanced responses to probe stimuli. (**A**) Schematic of the experimental protocol. Trials 2 to 13 began with an acclimatization phase of 8× optic flow pulses at 1 cm/s followed by a probe. (**B** to **E**) Average calcium responses in the backward-tuned cells to the different trials [(B), negative probe; (C), random stimulus timing followed by negative probe; (D), positive probe; and (E), no probe)]. The respective optic flow stimuli and average motor activity are shown above. Gray traces are the responses of individual fish ($N = 8$). Fold change in peak amplitude in response to the three presentations of the negative probe stimuli with respect to (w.r.t.) the baseline amplitude in trial 1 is shown for (B) and (C). $^*P < 0.05$ and $^{**}P < 0.01$ by Wilcoxon signed-rank test showing an elevation in amplitude w.r.t. baseline (dashed line at 0). There were no large calcium responses in the backward-tuned cells to the positive probe or the zero probe [(D) and (E)]. (**F**) Average calcium response in backward-tuned cells to the negative probe stimulus when presented in random order in trial 1 (gray) and to the first presentation of the same stimulus after acclimatization (black). (**G** and **H**) The peak amplitude in *dF/F* of the trial-averaged calcium response to the respective stimuli shown on the *x* axis for the backward-tuned cells (G) and the forward-tuned cells (H). $^*P < 0.05$ w.r.t. the baseline amplitude by post hoc Conover's test following a significant Friedman's test ($P = 3 \times 10^{-5}$). $n = 98$ cells, $N = 8$ fish in (G); $n = 41$ cells, $N = 7$ fish in (H). No large calcium events were seen in forward-tuned cells to any of the probe stimuli. Hence, no statistical analysis was performed to test for systematic changes in amplitude values across all trial types (see fig. S2).

In backward-tuned cells, after acclimatization, the response to negative probe stimulus showed a large amplitude increase compared to baseline (Fig. 3, B, F, and G). This enhanced response exhibited a decay over multiple presentations of the probe stimulus and approached baseline levels (Fig. 3, B and C). The increase in response amplitude was present to an equivalent extent when the timing of the acclimatization stimulus was randomized, indicating that timing did not play a role in the enhancement of the probe response (Fig. 3, C and G). Positive probe stimuli evoked no detectable calcium events in these cells (Fig. 3, D and G). In forward-tuned cells, negative probe stimuli evoked no response, whereas positive probe stimuli showed no enhancement with respect to baseline (Fig. 3H and fig. S2). Both forward-tuned and backward-tuned cells did not show any responses when stationary gratings were presented in the probe phase (Fig. 3, E, G, and H, and fig. S2C). Collectively, these results point to history-dependent enhancement of directionally tuned PC responses. Specifically, in backward-tuned PCs, weak backward flows during random presentation evoked a small response; the same stimulus after the fish was acclimatized with forward flows

evoked an enhanced response in the same PCs. It is possible that the enhanced response to the probe stimulus encodes a deviation from expected optic flow direction. On the basis of the above results, we hypothesized that the enhanced probe response is an error signal that the expected stimulus direction did not occur.

History-dependent PC responses report an unexpected external sensory event

Motor activity in closed loop often caused a sharp change in optic flow direction. We asked whether the enhanced probe response was also observed when the fish's own swimming resulted in comparable or larger backward grating movement. If a self-induced reversal of optic flow direction caused a comparable activation of PCs as the negative probe stimulus, then it would indicate that the response simply encoded a sensory change irrespective of what caused it. On the other hand, if the enhanced PC response to the negative probe stimulus represented an unexpected externally imposed change, then we would not expect to see strong activation in backward-tuned PCs.

As mentioned earlier, forward-moving gratings at 1 cm/s reliably evoked swims. Occasional swim bouts were observed in response to the positive probe stimulus in some fish. Both the negative probe stimulus and the stationary grating did not evoke swim responses (Fig. 4, A and B). In closed loop, the net optic flow stimulus presented to the fish is the difference between the externally provided optic flow stimulus and the virtual swim velocity of the fish (Fig. 4C) (see Materials and Methods). On average, the net optic flow stimulus seen by the fish showed a sharp dip below zero during swim bouts (Fig. 4D, top two panels), and the amplitude of the negative component was much greater during swims than the amplitude of the probe stimulus (Fig. 4, D and E, top two panels). The amplitude of the calcium response in backward-tuned cells to the motor activity–triggered reversal of optic flow direction was negligible compared to the response to the negative probe stimulus (Fig. 4, D and E, bottom traces).

To compare the two, we selected swim bouts that lasted 750 ms or more, corresponding to three calcium imaging frames, providing a sizable window for comparison of calcium activity. The average amplitude of the self-generated negative optic flow was much greater than the negative probe amplitude (Fig. 4, F and G). However, the amplitude of the calcium signal was greater in response to the probe stimulus than during swim events longer than 750 ms (Fig. 4H). Similarly, the slope of the calcium signal measured over three imaging frames from the onset of the probe stimulus was also greater than that in the case of swim events (Fig. 4I). These results show that sensory-tuned PCs are not activated by self-generated sensory input. The enhanced response to the negative probe stimulus encodes an externally triggered deviation in expected optic flow direction. Thus, these enhanced "Post" responses could represent a prediction error in what the next stimulus is going to be. We test this idea further in the following experiments.

PC response to probe represents the magnitude of error from the expected stimulus pattern

If fish learnt what stimulus to expect, then we hypothesized that the level of confidence that they have in what to expect from the sensory world would be reflected in a correspondingly scaled enhancement of the PC response to deviant stimuli. To test this hypothesis, we designed an experiment where we attempted to induce varying levels of confidence by varying the number of repetitions of the acclimatization stimulus. In this experiment, in trial 1, we presented forward and backward flows in random sequence as we did before (Fig. 2C) to identify the directional tuning of PCs. Following this, we presented a series of trials in which we presented three negative probe pulses followed by varying numbers of repetitions of forward optic flow (1 cm/s) and ending with three negative probe pulses again (Fig. 5A). In each trial, we set the number of repetitions of the forward optic flow at 2, 4, 8, or 16 pulses and interspersed these trials in random order. The trials were separated by a 30-s intertrial interval (ITI) during which stationary gratings were presented.

We identified backward-tuned PCs from their responses during trial 1 and then analyzed the responses of these cells to the negative probe stimuli occurring before the repetitive forward optic flow stimuli ("Pre") and those occurring after ("Post"). There was no change in the Pre response amplitude across all trials (Fig. 5, B, left, and C). The Post responses scaled with the number of repetitive pulses (Fig. 5, A to D). The response amplitude to the first probe pulse in the Post phase increased on average twofold with increasing number of repetitions of the acclimatization stimulus (Fig. 5D and fig. S3). The scaling was nonlinear, and the population average followed a logarithmic trend. The increase in amplitude was visually apparent starting from two acclimatization pulses and became statistically significant with four or more pulses. This scaling could also be observed in the responses of individual cells (fig. S3). The scaling approached saturation at 16 acclimatization pulses (Fig. 5D).

The neural encoding of the unexpected stimulus scaled with acclimatization, indicating that the fish have acquired a representation of the consistency in the stimulus pattern in their environment. We then asked whether this expectation of the forward optic flow stimulus contributes to lowering response latency and whether the modulation of latency due to the probe stimulus, as seen in Fig. 1C, also scales with the number of acclimatization pulses. Specifically, we would expect that as the number of acclimatization pulses increase, the latency would decrease. In addition, following a probe, the latency would be modulated upward more strongly for greater repetitions as the probe is violating a stronger prediction. The imaging experiment (Fig. 5, A to D) did not contain enough number of trials for reliably estimating latency modulation due to acclimatization. We therefore recorded behavior without imaging in a separate set of fish where we could measure responses to up to 15 repeats of each acclimatization trial. In this experiment, fish were presented with a scrambled sequence of weak stimuli followed by either 2×, 4×, or 8× forward optic flow stimuli (fig. S4A). After acclimatization, a single probe stimulus, followed by a "test" forward optic flow stimulus, was presented. The test stimulus was 4 s in duration, in contrast to the 2 s of the other stimuli. The 4-s duration allowed us to more reliably measure the full extent of latency increase following the probe stimulus. Latency modulation, however, was computed for trials with latencies ≤ 2 s in the test stimulus pulse to allow fair statistical comparison of modulation values across pre-probe stimuli that were 2 s in duration.

The latency to respond to the first acclimatizing pulse was high for all trials (fig. S4, B and D), following which the latency dropped significantly for the rest of the pulses in the trial (fig. S4, B and D),

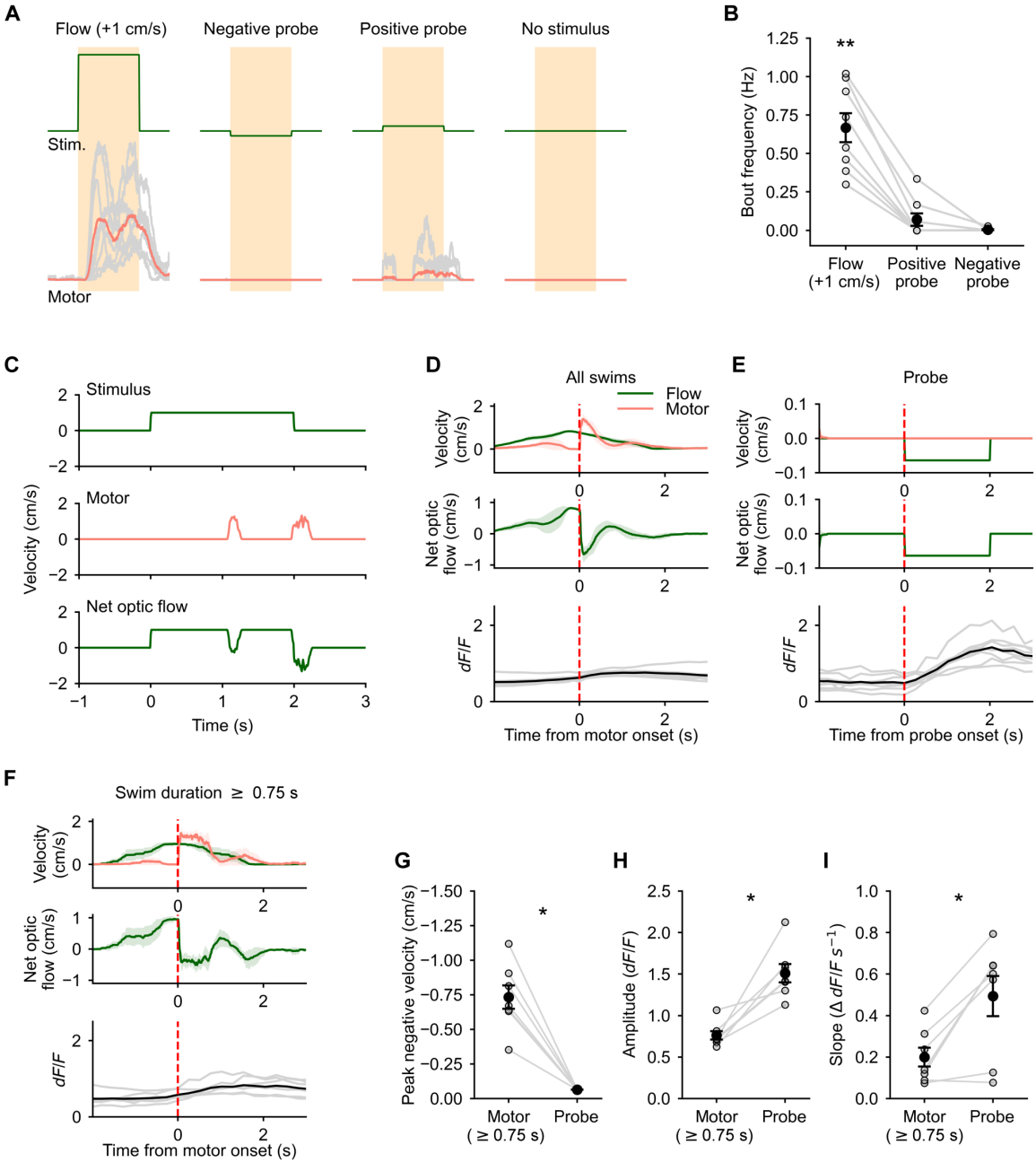

Fig. 4. Self-induced change in optic flow direction does not cause Purkinje cell (PC) activation. (**A**) Average motor activity (bottom, red) during forward optic flow at 1 cm/s, negative probe, positive probe, and no optic flow stimuli (top, green). (**B**) Forward optic flow reliably evoked swims, whereas very few and no swims were seen in response to positive probe and negative probe stimuli respectively. $N = 8$ fish, $^{**}P = 0.0006$ by Friedman's test, $P = 0.011$ (forward flow versus +ve probe) and $P = 0.002$ (forward flow versus −ve probe) by post hoc Conover's test. (**C**) Example forward optic flow stimulus at 1 cm/s (top), motor activity (middle), and the resultant net optic flow experienced by the fish in closed loop (bottom). (**D**) Motor onset triggered average optic flow stimulus (green, top), swim velocity (pink, top), and net optic flow experienced by the fish (middle). Bottom panel shows average calcium responses in backward-tuned PCs aligned to motor onset. (**E**) Probe triggered average optic flow (green, top), swim velocity (pink, top), and average net optic flow experienced by the fish (middle). Bottom panel shows the average calcium responses in backward-tuned PCs aligned to probe onset. (**F**) Same as (D) for swim events lasting longer than 0.75 s. (**G**) Magnitude of the negative component of optic flow during swims is much larger than the amplitude of the negative probe stimulus. (**H**) Peak amplitude of the calcium response in backward-tuned cells to the negative probe stimulus is much larger than the response to swim bouts. (**I**) The slope of the rise phase of the calcium response in backward-tuned cells is significantly steeper for the negative probe stimulus than during motor activity. $N = 7$ fish, $^{*}P = 0.016$ [(G) and (H)] and 0.03 (I) by Wilcoxon signed-rank test. Shaded areas in (D) and (F) represent SEM across eight fish.

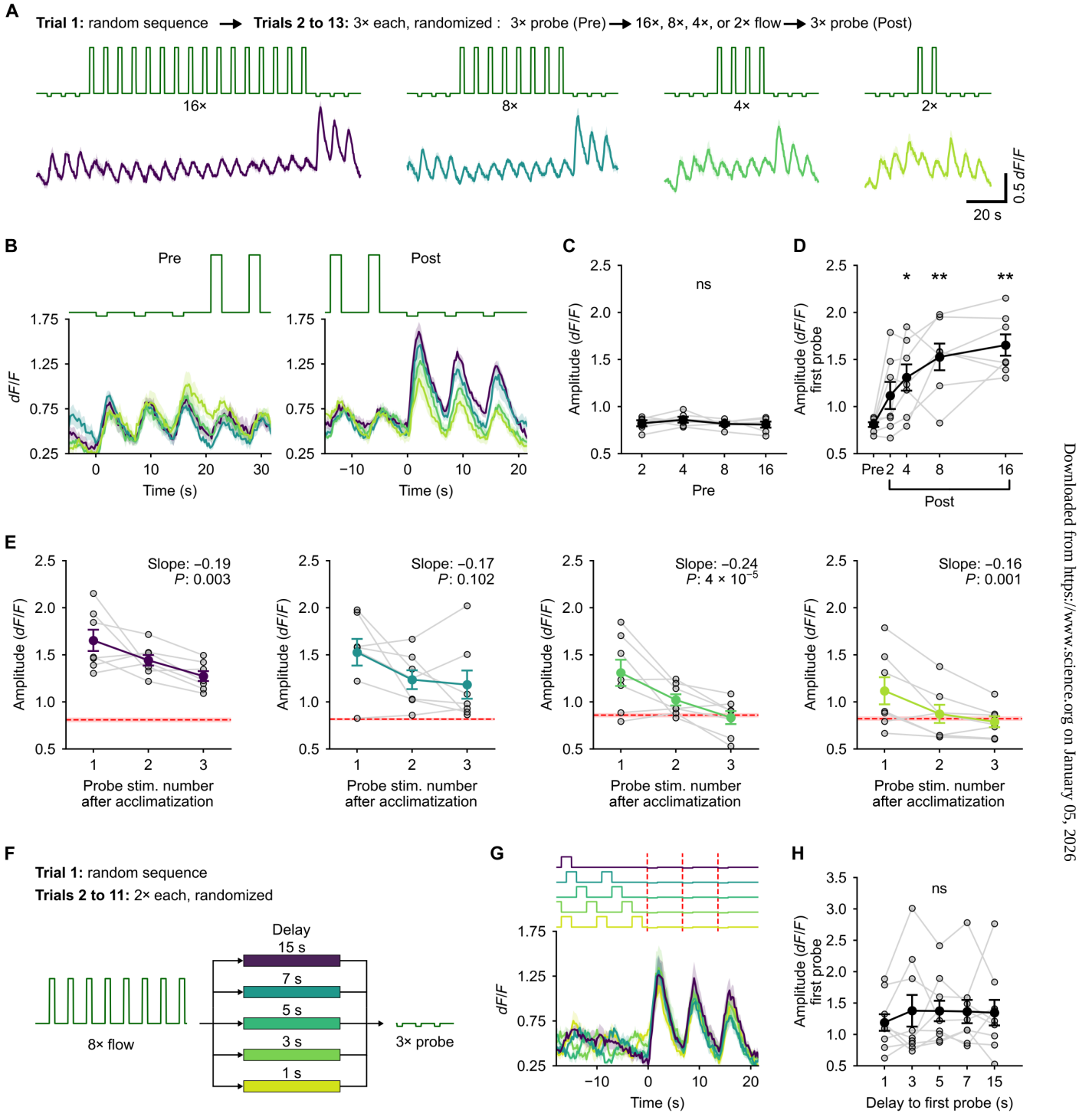

Fig. 5. Purkinje cell (PC) response to probe represents the magnitude of error from the expected stimulus pattern. (**A**) Top (text): Description of the experimental protocol. Middle: Stimulus traces. Bottom: Corresponding calcium responses in backward-tuned cells. Solid line is the mean for $N = 7$ fish, and shaded regions are SEM. Colors indicate the number of acclimatization pulses. (**B**) Zoomed-in view of the average calcium response of backward-tuned cells to pre-probe (left) and post-probe (right) pulses aligned to the onset of the first probe. (**C**) Average amplitude of the response to pre-probe stimuli. ns, $P = 0.54$. The three probe pulses were pooled as there was no difference between them. (**D**) Average amplitude of the response to the first post-probe pulse scales with the number of acclimatization pulses. $P = 0.0015$ by Friedman's test; $^*P < 0.05$ and $^{**}P < 0.01$ by post hoc Conover's test w.r.t. the pre-probe amplitude. (**E**) Decay of the amplitude of the enhanced response to the post-probe stimulus over the three successive post-probe pulses for the different number of acclimatization pulses. Red dashed line with the shaded region shows the mean and SEM of the respective pre-probe amplitudes. Slope and P value by linear mixed-effects are inset in each plot. (**F**) Schematic of the experimental protocol for the delayed probe experiments. 3× probe pulses were presented with a variable delay from 1 s to 15 s after 8× acclimatization pulses. (**G**) Average response of the backward-tuned cells aligned to the onset of the probe pulses. Shaded regions are SEM across $N = 9$ fish. Colors indicate the delay as shown in (F). (**H**) Amplitude of the response to the first probe pulse does not depend on the delay. ns, $P = 0.98$ by Friedman's test.

suggesting that fish respond faster when the stimulus they expect is what occurs. As seen earlier (Fig. 1C), latency was significantly longer in the test stimulus pulse and increased with increasing number of acclimatization pulses (fig. S4, B to E). These results suggest that the neural encoding of both stimulus consistency and unexpected deviations from recent stimulus history contribute to the modulation of latency of the OMR.

We next wanted to test whether the enhanced Post responses that we observed in PCs after acclimatization with four or more repetitive forward optic flow pulses could be explained by alternate mechanisms not involving the generation of predictions. First, we asked whether the enhancement is dependent on elapsed time between the Pre and Post negative probe pulses. Negative probe pulses separated by 35 s of stationary gratings caused no enhancement of responses, whereas presentation of four forward optic flow pulses within that same time window caused significant enhancement of Post responses (fig. S5). These results indicate that the enhancement of PC response to probe depends on repetitive experience with the acclimatization stimulus, suggesting that fish have formed an experience-based expectation of what stimulus they are likely to encounter.

Second, we asked whether the enhancement was dependent on encountering forward optic flow multiple times or is it dependent on encountering it for longer periods of time. To answer this question, we presented a separate set of fish with a constant forward optic flow stimulus at 1 cm/s in the acclimatization phase for an equivalent time duration as in the pulsed acclimatization experiments (fig. S6A). A constant optic flow acclimatization stimulus did not lead to an enhanced Post response with respect to Pre responses (fig. S6, B to D), and the Post responses were significantly lower in amplitude than the corresponding pulsed acclimatization stimuli (fig. S6E). These results show that the underlying mechanism is not based on a simple integration of sensory input with long time constants. Rather, multiple presentations of the same stimulus, forward optic flow in this case, strengthen the expectation of such stimuli and enhance responses to probe stimuli. If this was the case, then we expected two properties to be exhibited by the Post response. First, multiple presentations of the probe stimulus would lead to a decay of the enhanced response until it comes back to the baseline sensory response amplitude. Second, the process that generates enhanced Post responses must require novel experience to be updated and not decay on its own. If the fish receives no new stimuli, then no updates to previously generated predictions should be seen.

When we looked at the Post responses of 2×, 4×, 8×, and 16× acclimatized larvae, there was a significant decay in amplitude from the first to the third presentation of the probe stimulus in all four conditions (Fig. 5E). For the 2× and 4× conditions, the amplitude of the Post response decayed back to the Pre levels (Fig. 5E, right two panels), while, in the 8× and 16× conditions, the third Post response decayed significantly compared to the first but was still enhanced compared to Pre (Fig. 5E, left two panels). An obvious explanation for this is that the 8× and 16× pulses cause greater enhancement of the Post responses, but the rate of decay after repeated probe presentations is the same across the four conditions. This is evidenced by the similar line slopes seen in Fig. 5E.

Next, to test whether the predictions generated by acclimatizing stimuli decay with time or if it requires novel experience, we conducted a separate experiment on a different group of fish. Fish were acclimatized to eight pulses of forward optic flow at 1 cm/s, followed by three probe stimulus pulses, separated by 5 s each, as in earlier experiments. The delay to the first probe pulse from the last acclimatization pulse was varied from 1 to 15 s as shown in Fig. 5F. The amplitude of the response to the first probe pulse was independent of the delay from the acclimatization phase (Fig. 5, G and H) and exhibited a decay over the three repeats of the probe stimulus (Fig. 5G and fig. S7). These results show that the expectation is updated with experience and does not decay with time, within the limits of the 15-s window. There being no change in amplitude of the response to the first probe also suggests that fish learn what stimulus they are likely to encounter rather than the time at which it would occur.

Together, the above results suggest that larval zebrafish learn to expect optic flow stimuli they are likely to encounter based on stimulus history over minute timescales. A deviant probe stimulus caused enhanced responses in PCs, which scaled with the number of repetitions of the acclimatization stimulus. This enhanced response decayed back to baseline with repeated presentations of the probe stimulus and represents an error in expectation, which is likely to play a role in updating predictions of the sensory world as new evidence is encountered.

GCs encode actual and predicted sensory input but not prediction errors

PCs receive excitatory inputs from two distinct synaptic pathways, namely, PFs from cerebellar GCs and CFs from the IO. It is believed that GCs encode sensory context and motor activity, whereas the CF pathway carries reinforcing error signals. PF synapses coactive with the error signal are suppressed by long-term depression, and those decorrelated with error selectively contribute to PC activity, subsequently affecting behavior. According to this framework of cerebellar function, we would expect GCs to represent an array of sensory-tuned responses but not the error in expected optic flow direction.

We next asked what features of actual and predicted visual input could be represented in GC input to PCs. We performed serial volumetric calcium imaging of the GC population expressing GCaMP6f under the neurod promoter (Fig. 6, A and B). A single hemisphere of the cerebellum was densely sampled across six imaging planes separated by 10 μm, yielding a total of 6465 GCs across eight fish. This accounts for ~27% of all GCs in one hemisphere of the 7-day-old larval zebrafish cerebellum. The stimulus protocol consisted of two trials separated by 30 s. The first trial was a randomized sequence of stimulus pulses to determine baseline responses of GCs to optic flow, as was done for PCs. The second trial began with eight acclimatization pulses of 1 cm/s followed by three negative probe pulses and then three pulses of 1 cm/s and ended with an equivalent period of stationary grating (Fig. 6A).

We then used correlation-based hierarchical clustering to identify functional GC response types (Fig. 6, C to G and I). Clustering was performed independently for each fish using activity traces from the second trial. The number of clusters per fish was set to 5 with the help of silhouette plots. The clusters were then assigned names based on the relationship of the observed response types to the optic flow stimulus. The same response types were not present across all fish but were largely overlapping (Fig. 6, C to G and I).

A substantial proportion of cells (43%) were either inactive or sparsely active in a nonstimulus selective manner (Fig. 6F). Fifteen

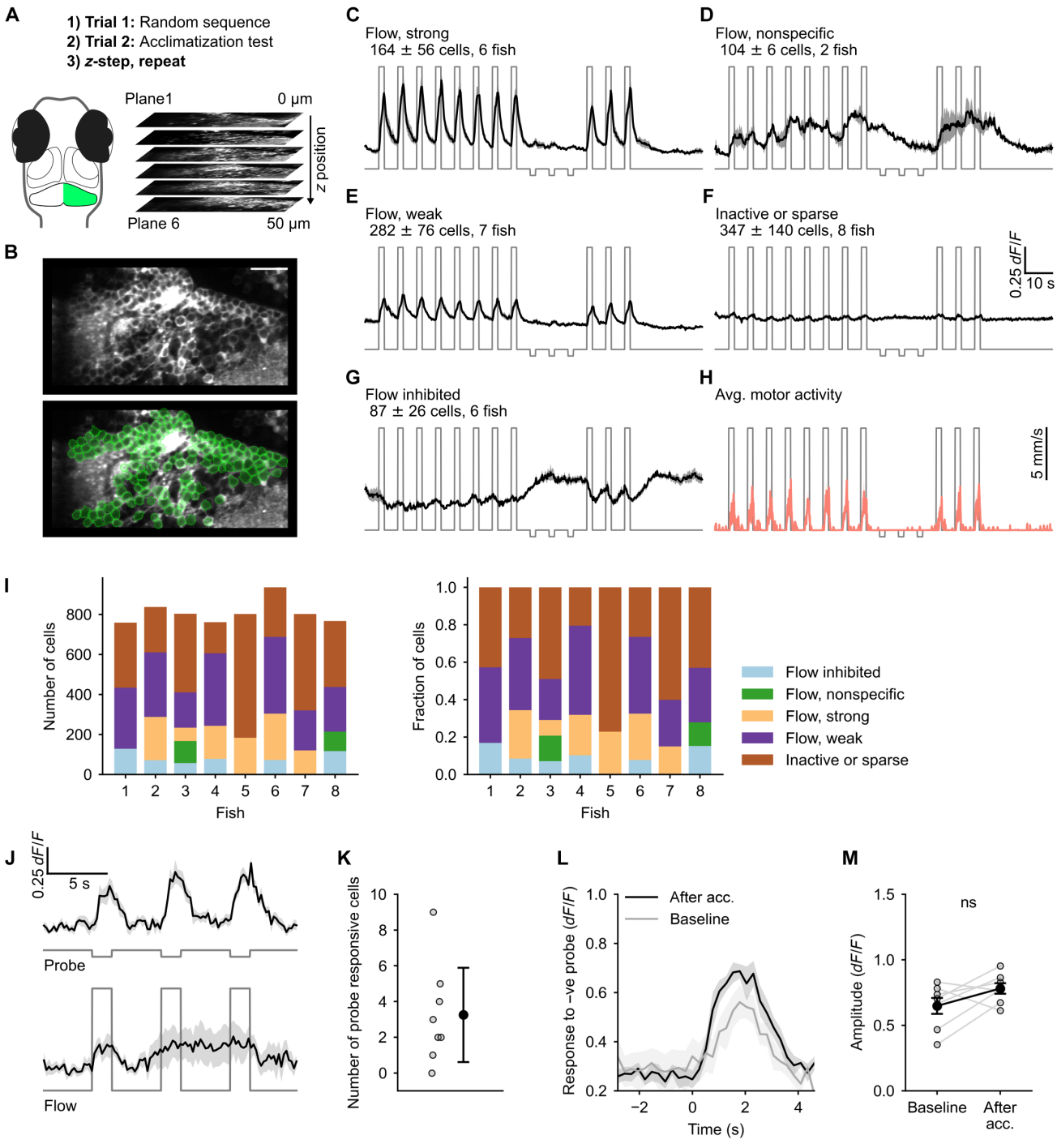

Fig. 6. Granule cell (GC) responses reveal absence of the error signal. (**A**) Schematic of the experimental protocol. (**B**) A representative imaging plane (top) and regions of interest (ROIs) drawn around GC cell bodies using semiautomated anatomical segmentation (bottom). Scale bar, 20 µm (**C** to **G**) Functional response types identified using correlation-based clustering. The cluster label, the number of cells (means ± SD), and the number of fish in which the cluster was found are inset in each panel. (**H**) Average motor activity overlaid on the optic flow stimulus trace. (**I**) The number and relative proportions of GCs in each cluster across fish. (**J**) Top: Response of probe responsive cells identified using cross-correlation with stimulus regressor. Bottom: Response of the same cells shown on top to optic flow at 1 cm/s. (**K**) Number of cells identified as probe responsive. (**L**) Average response of the probe responsive cells to negative probe pulses after acclimatization and when presented at random (baseline). (**M**) Response amplitude of the probe responsive cells to negative probe when presented randomly compared to the amplitude after acclimatization. ns, $P = 0.11$ by Wilcoxon signed-rank test. Traces shown in (C) to (H), (J), and (K) are means ± SEM.

percent of all cells were strongly tuned, and an additional 31% were weakly tuned to the forward optic flow stimulus, respectively (Fig. 6, C and E). Three percent of all cells were activated nonspecifically by forward optic flow and exhibited a persistent elevation in calcium activity outlasting the stimulus and/or motor activity (Fig. 6D). The final cluster consisting of 8% of the sampled GC population included cells that were inhibited by forward optic flow and showed elevated activity when forward optic flow was stopped. This elevation in activity was unrelated to probe stimuli and was seen even with stationary gratings (Fig. 6G). No response type was found tuned to the weak probe stimulus, indicating that the large-amplitude responses observed downstream in the PC population were not caused by GC activity.

It is possible that the clustering method failed to identify a sparse subset of GCs tuned to the negative probe stimulus. To address this, we explicitly looked for cells showing responses to the three pulses of the negative probe stimuli by cross-correlating a short segment of the calcium trace around the probe pulses with the stimulus regressor (Fig. 6J). By setting a conservative threshold correlation of 0.5, we were able to find 3 ± 3 cells (means ± SD) per fish that were tuned to the negative probe stimulus (Fig. 6, J, top, and K). Because the responses were not trial-averaged, lower thresholds than 0.5 picked up correlated imaging noise. Cells identified using this method were not activated by the flow stimulus at 1 cm/s (Fig. 6J, bottom). However, they had comparable response amplitude to the negative probe stimulus when presented in random order in the first trial (Fig. 6, J and M), suggesting that this is a sensory representation of the probe stimulus. The absence of enhanced responses to probe after acclimatizing with forward flow stimuli strongly suggests that the error responses most likely arrive from the IO.

Stimulus expectation is driven by simple-spike and CF modulation in PCs

The above results show that GCs convey sensory representation of flow and probe stimuli to PCs. Our data also show that repeated forward optic flow presentation is integrated by GCs to generate a slowly rising signal that outlasts the flow duration (Fig. 6D). Such GC inputs will be expected to modulate simple-spiking in PCs. To determine whether there is flow-driven and expectation-driven simple spike (SS) modulation, we performed loose-patch recordings in PCs while presenting repeating forward optic flow pulses. We then performed loose-patch extracellular recordings from PCs in paralyzed fish presented with repetitive forward optic flow stimuli (Fig. 7A). Of the 20 cells recorded, all of them showed strong activation during forward optic flow. All 20 cells showed a strong SS rate increase during forward optic flow stimuli, and 15 of the 20 showed a strong increase in CF input rate. In these cells, we saw a significant increase in SS rate (Fig. 7B) and, unexpectedly, CF input rate (Fig. 7C) in a 3-s window leading up to the onset of forward optic flow. Thus, both SSs and CFs seem to signal an expectation-driven component in PC activity.

Strong population-wide encoding of expectation and error correlates with lower swim latency

On the basis of the above, we proposed that, when forward optic flow stimuli are presented repeatedly, a population of CFs and GCs might relay predictions to PCs via their slowly ramping up signals. A separate population of GCs encodes actual flow information. Likewise, when a probe stimulus occurs after a series of forward optic flow pulses, GCs signal the occurrence of probe stimulus while CFs relay a prediction error signal to PCs. We propose that PCs might use these information streams to update existing predictions. Thus, these circuits likely underlie the cerebellum-dependent modulation of swim latency after probe trials (Fig. 1, C and D). Therefore, we imaged PC activity using the same trial structure as in Fig. 1 and investigated the relationships between PC activity and swim latency.

Again, we sorted cells into forward- or backward-tuned on the basis of their average calcium responses to each of the stimuli. An average response profile was constructed for each cell by stitching together the average response to forward optic flow and probe (Fig. 7D). Using regression, we then classified cells as either forward-tuned (Fig. 7D, purple) or backward-tuned (Fig. 7D, black). Because there were 90 pulses of forward optic flow and 10 of probe, we obtained a good classification using a threshold correlation of 0.4 as imaging noise was averaged out effectively. Of the 1874 total cells from 27 fish, 478 were backward-tuned and 1248 were forward-tuned.

First, we asked whether the population-wide pre-flow calcium signal, corresponding to the ramping SS and CF inputs, was predictive of swim latency. Where the PC population encodes a strong prediction, the swim latency will be expected to be lower and vice versa. For this analysis, we extracted the average pre-flow dF/F for both forward- and backward-tuned cells and fit a linear mixed-effects model between swim latency and the pre-flow calcium activity. The pre-flow calcium activity in forward-tuned cells showed a significant negative correlation with latency (Fig. 7E). A significant negative correlation could be detected up to ~2.5 s before the onset of the stimulus (Fig. 7H). The correlation was absent when stimulus order was shuffled (Fig. 7F) and was not present in cells tuned to the backward direction of optic flow (Fig. 7G). This observation is consistent with the idea that the cells active during forward optic flow are likely the ones involved in the generation of behavioral responses, and, hence, any representation of an expectation of forward optic flow that contributes to behavior is therefore also present in their pre-flow activity and not in the backward-tuned cells.

Next, we asked whether the same is also true for population-wide representations of prediction error. We have shown that, as confidence in expected stimulus pattern increases, the amplitude of PC response to an unexpected probe stimulus also increases (Fig. 5). This means that strong prediction error responses in PCs will be expected to negatively correlate with swim latencies in trials around the probe trial because the probe trial itself does not evoke swims. We looked at both the population-averaged amplitude and the probability of occurrence of large calcium transients in response to probe stimuli in backward-tuned cells—a high amplitude or probability would imply higher confidence in the expected stimulus pattern and vice versa. Response probability was estimated by counting the occurrence of a large calcium event (>3 SDs from baseline) during probe pulses. Because probe stimuli were presented in only 10% of the trials, we linearly interpolated the amplitude and probability to obtain coarse-grained readouts across the 100 stimulus pulses (Fig. 7, I and J). Similarly, latency values were also linearly interpolated and smoothened with a rolling average spanning 10 stimulus pulses. Fish that paused swimming for a continuous sequence of 10 or more pulses were excluded to minimize interpolation artifacts. The 10 pulse long smoothing window matched the average distance

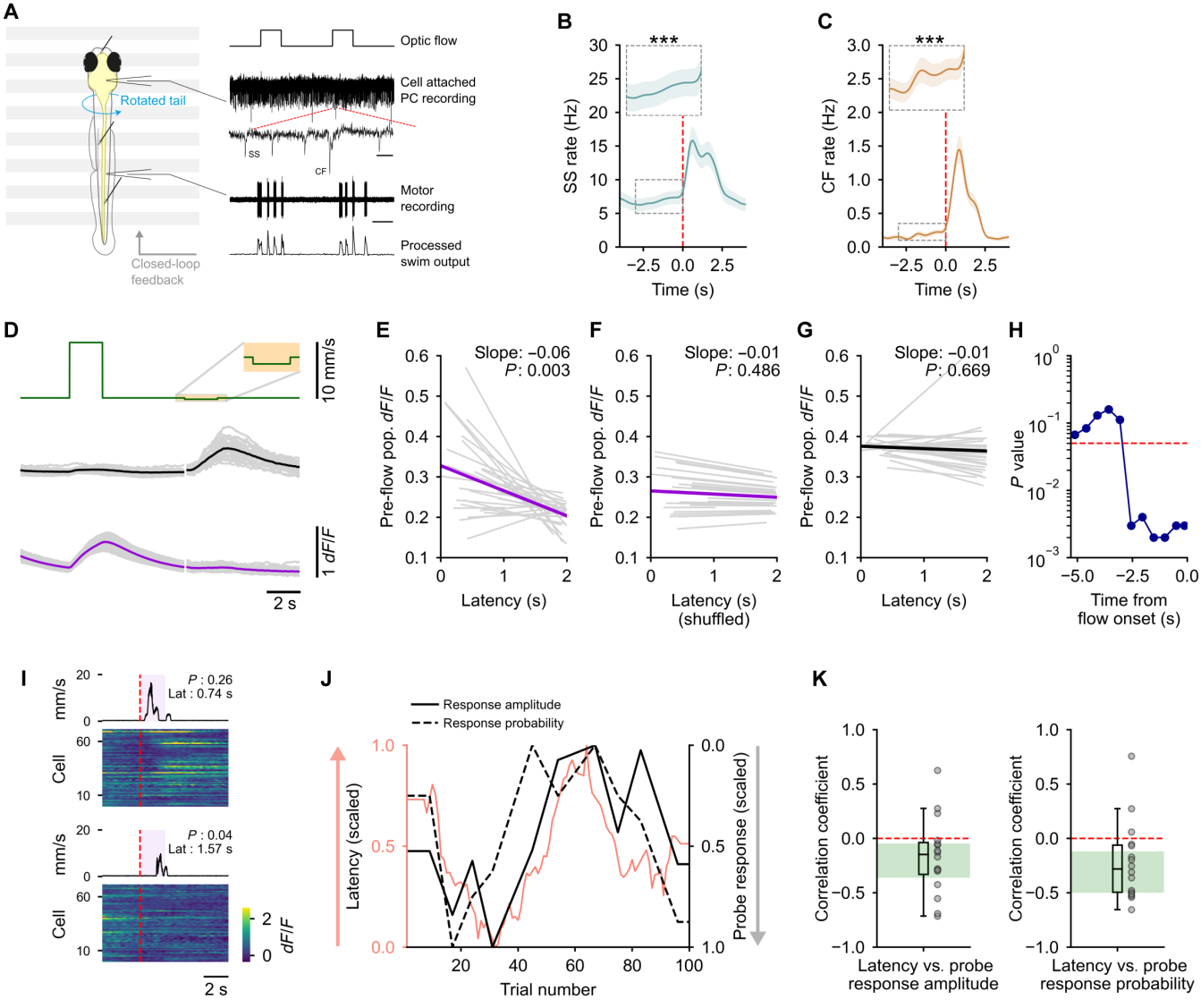

Fig. 7. Strong population-wide representation of stimulus expectation correlates with lower swim latency. (**A**) Left: Schematic of the experimental preparation. Right: Traces showing the optic flow stimulus, PC recording with SSs and CF inputs, fictive motor recording, and the processed motor signal used for closed-loop feedback for some fish. Scale: zoomed-out, 2 s; zoomed-in, 20 ms. (**B** and **C**) Both SS (B) and CF input (C) rates show a significant, steady increase before the onset of optic flow. ***$P < 0.001$ by linear mixed-effects. $n = 20$ cells in (B) and $n = 15$ cells in (C). (**D**) Regression-based classification of cells into forward (magenta)– and backward (black)–tuned. Gray traces represent individual fish, $N = 27$. (**E** to **G**) The pre-flow calcium activity is significantly anticorrelated with latency for the forward-tuned cells (E). No correlation is seen after shuffling trial order (F) or in backward-tuned cells (G). Slope and P value by linear mixed-effects are inset in each plot. $N = 27$ fish. (**H**) The pre-flow calcium activity in forward-tuned cells is significantly anticorrelated with latency up to 2.5 s before the onset of the forward optic flow stimulus. (**I**) Heatmap of single-trial responses of all cells in a representative fish to two instances of the negative probe stimulus. The average motor activity over a window of 10 nonprobe stimulus pulses around each of the probes is shown on top. The mean latency to initiate swims and the population-wide probe response probability are inset in each plot. (**J**) Representative plot from one fish showing latency to swim in response to forward optic flow (pink) along with probe response amplitude (black) and probability (black dashed) for backward-tuned cells. (**K**) Both amplitude and probability are anticorrelated with latency. Green-shaded area shows 95% confidence interval for the median estimated by bootstrapping. $N = 16$ fish.

between two probe stimuli, thereby yielding a comparably coarse-grained estimate of latency. We then proceeded to compute the Pearson's correlation coefficient between these population-wide readouts of how strongly fish expected forward optic flow and the latency to swim. Swim latency was negatively correlated with both amplitude and response probability (Fig. 7, J and K). These results suggest that population-wide representations of predictions and prediction errors in PCs feed into the motor planning process and drive faster motor responses to predictable stimuli.

DISCUSSION

Here, we have shown that larval zebrafish are capable of learning patterns of sensory input and generate predictions using sensory evidence integrated over minute timescales. When current sensory input does not match predictions, they are able to update the incorrect predictions such that future errors are minimized. Predictions of optic flow stimuli feed into the motor planning process and contribute to lower latency swim responses. We show that the cerebellum is an integral part of circuits underlying the generation and

updating of sensory predictions and motor planning. Our data show that PCs receive predictive signals from GCs and from the IO while they receive prediction error signals exclusively from the IO. Using these prediction and prediction error signals, PCs update existing predictions so as to adapt behavioral output.

Using two-photon calcium imaging in head-restrained larval zebrafish in a closed-loop optomotor environment, we identify and characterize a previously unknown expectation-based component involved in the OMR. Our results show that, with experience, fish learn to expect the direction of optic flow stimulus in a cerebellum-dependent manner (Fig. 1). PCs in the cerebellum show directionally tuned strong optic flow responses (Fig. 2). In addition to encoding sensory input, the PC response to optic flow included a component that encoded the degree of unexpectedness of the stimulus while maintaining direction tuning (Figs. 3 and 5). These responses were not observed when stimulus movement was caused in closed loop by the larva's own swimming (Fig. 4), indicating that these responses reflected the "unexpectedness" of the stimulus. As seen in other systems (*2*, *6*, *19*), we propose that this nonsensory component constitutes an error signal that is critical for maintaining an updated belief of what to expect from the sensory world. Activity in the GC population revealed a variety of sensory-tuned responses but not the error signal, indicating that CF inputs from the IO convey error information to PCs (Fig. 6). A subset of GCs exhibited a persistent stimulus-tuned response, which possibly encodes stimulus expectation (Fig. 6, D and G). An error-driven learning rule could enable PCs to incorporate appropriate predictive signals from GCs to modulate behavior. The PC population-wide encoding of predictions as well as prediction error correlated negatively with swim latency, suggesting that stimulus expectation might contribute to lowering the latency of swim responses (Fig. 7, D to K). In sum, these results point to a central role for the cerebellum in signaling deviations from expectation and in sculpting motor responses for expected and unexpected stimuli.

Role of the cerebellum in zebrafish optomotor behavior

Previous studies have identified the larval zebrafish pretectum as the primary optic flow processing region involved in the OMR (*27*, *38*). The cerebellum receives inputs from direction-tuned neurons in the pretectum (*38*), but a direct role for the cerebellum in sensorimotor transformations involved in the OMR has not been identified (*27*, *38*). Here, we show that lesioning the cerebellum does not affect the response latency or swim probability (Fig. 1, F and G). However, unlike control fish, the lesioned fish were not perturbed by an unexpected change in optic flow direction (Fig. 1, C and D), suggesting an inability to incorporate an expectation of optic flow direction into the OMR. This shows that the cerebellum does not play a direct role in the generation of the response but is rather involved in biasing behavior based on past experience.

Dense and persistent sensory representations in GCs

The 7-dpf larval zebrafish cerebellum consists of around 6000 GCs that converge onto 300 PCs. In our experiments, we sampled ~27% of GCs in one hemisphere per fish. Our observation of dense activation of the GC population in response to optic flow stimuli (Fig. 6, C to G) is consistent with the recent findings from larval zebrafish (*39*, *40*) and other species (*17*, *41*). We also found response profiles in the GC population exhibiting stimulus-tuned but persistent elevation in calcium activity (Fig. 6, D and G). One of these response profiles, present in six of the eight fish (Fig. 6G), was inhibited strongly by forward optic flow and showed long-lasting elevation during periods of no optic flow or probe. It is possible that sensory expectations could be encoded in persistent activity of such a subpopulation. A recent study of GC responses to luminance changes in larval zebrafish also found temporally diverse and persistent activity lasting tens of seconds from stimulus onset (*40*). Depression of GC inputs coincident with error signals from the IO would allow PCs to select response profiles that contribute to error-free behavior.

Error signals encoded in CF inputs from the IO

PC calcium signals arise from bursts of SSs driven by GC input and/or by CF input. Because no error representation was present in the GC calcium responses, although a substantial proportion of them were sampled (Fig. 6), the error signal that we see in the PC population likely is encoded in CF inputs from the IO. It is therefore possible that PC direction tuning (Fig. 2E) determined by calcium imaging reveals how error signals are tuned for each cell rather than their sensory tuning. Future experiments to determine how error maps onto GC input will provide important insights into cerebellar computation.

How the brain generates error signals has been a long-standing question in neuroscience. To generate error, there must already be a prediction or an expectation that is compared with ground-truth sensory input to determine whether there are mismatches. This error can then be used to update the expectation such that future errors are minimized. In the findings presented here, the error signal is most likely computed by or relayed to IO neurons, which then map onto PCs in the cerebellum. This would indicate that neurons encoding the expected direction of optic flow, either as persistent activity or distributed across the network, are present upstream of the cerebellum.

Integration of sensory expectations and error by PCs and their influence on behavior

Individual PCs receive convergent input from a large number of GCs, possibly composed of a variety of different response types. We hypothesize that PCs implement an error-driven learning rule that adaptively scales the contribution of GC response types to behavior. Specifically, the inputs to PCs from GCs encoding stimulus expectation that are active during probe get progressively suppressed, thereby contributing less to generating the behavioral response. Multiple observations presented here are consistent with this model. (i) The expectation is updated only when stimuli that are either consistent (repeated forward flow) or inconsistent (deviant probe flow) with the past are experienced (Fig. 5). Extended periods of no optic flow do not lead to a change in the amplitude of the error response (Fig. 5G and fig. S3), nor does constant optic flow (fig. S4). These results point toward an experience gated updating process. (ii) The latency to swim in response to forward optic flow is negatively correlated with the prevalence of error encoding in the PC population (Fig. 7, I to K). Furthermore, the response latency is longer immediately following a probe pulse compared to the pre-probe baseline (Fig. 1C), but no elevation is seen in cerebellum lesioned fish (Fig. 1D). This suggests that stimulus expectation might contribute to a lower latency OMR.

While the model proposed here provides an algorithmic description of the neural mechanism, it opens up several questions for further investigation. As discussed above, for an error signal to be

computed, a comparison between an expectation and ground truth is necessary. It is unclear how the brain acquires this expectation and how it is encoded in neural activity. Examining the activity of IO neurons and the inputs they receive will shed light on this process. In addition, the role of the cerebellum may not be limited to tuning the influence of expectation on behavior generation. Cerebellar feedback to upstream brain regions could play an important role in acquiring these expectations. Last, the output of the cerebellum does not directly cause movements. It remains to be seen how cerebellar output integrates with sensorimotor computations involved in generating the OMR.

Ethological relevance of predicting optic flow

Shallow water streams inhabited by larval zebrafish often show repetitive and predictable changes in flow due to water waves or vortex streets shed by objects intercepting laminar flow. Fast and precise reactions to these perturbations caused by flowing water are likely to prevent fish from being washed away from a favorable environmental niche. In our experiments, fish learnt to expect optic flow direction with minimal prior exposure and continuously adapted their expectation with experience. Such an adaptable predictive mechanism functioning on timescales of immediate behavioral requirements is highly relevant in the natural setting. In addition to this homeostatic function, it is possible that fish incorporate predicted environmental perturbations to fine-tune other behavioral responses such as escape swims or prey capture maneuvers, such that the motor command generated in these situations compensates for displacement due to expected flow patterns. This study sets up an ideal model to investigate how multiple parallel predictive mechanisms involved in expecting flow-induced perturbations and those involved in behaviors such as escape or prey capture work in concert to ultimately guide appropriate behavioral choices.

MATERIALS AND METHODS

Fish

We used 6- to 8-dpf zebrafish (*Danio rerio*) larvae for all experiments. The larvae were raised in E3 medium (composition: 5 mM NaCl, 0.17 mM KCl, 0.33 mM $CaCl_2$, 0.33 mM $MgSO_4$, and 0.5 mM methylene blue) or fish facility water with 0.5 mM methylene blue, at 28.5°C in accordance with standard protocols (https://zebrafish.org/home/guide.php). *Tg(aldoca:GCaMP6s);nacre*$^{-/-}$ larvae (from M. Hibi, Nagoya University, Japan) and *Tg(neurod:GCaMP6f);nacre*$^{-/-}$ larvae (from C. Wyart, I.C.M., Paris) (*42*), outcrossed into the Indian wild-type (from local aquarium suppliers) background, were used for experiments involving two-photon imaging. Indian wild-type larvae were used for electrophysiological recordings. Each experiment was spread out over at least three different batches of larvae. All experimental procedures were approved by the Institutional Animal Ethics Committee of the National Centre for Biological Sciences.

Experimental preparation

For experiments involving two-photon imaging, 7- to 8-dpf zebrafish larvae were anesthetized by briefly immersing them in 0.017% MS-222 (Sigma-Aldrich) and embedded dorsal side up in a drop of 2% low–gelling temperature agarose (Sigma-Aldrich) placed in the center of a 60-mm petri dish lid. The dish was filled with E3 medium, and the tail below the level of the swim bladder was freed from agarose. The embedded fish were allowed to recover for 4 to 8 hours before the experiment.

Real-time motor output detection for closed-loop optomotor feedback

Custom Bonsai workflows (*43*) were used for real-time motion detection. The algorithm used by our software for online motion detection closely matched previously published protocols (*28*, *44*). Video-based motion detection was done at 200 frames per second (fps) using a Flea3-USB3.0 camera (FLIR). The tail of the fish was illuminated from one side by a collimated 780-nm light-emitting diode (LED) (M780D2, Thorlabs) and imaged onto the camera sensor below, using a reversed Nikon 50-mm f/1.8d lens with a 24-mm extension tube for increased magnification (Fig. 2A). Both the illumination and imaging light paths were filtered through 780-nm band-pass filters (FBH-780-10, Thorlabs). The imaging light path was filtered to exclude light from the visual stimulus and two-photon laser, and the illumination light path was filtered to block low-intensity visible light emission from the 780-nm LED (Fig. 2A). Real-time motion detection was performed by frame subtraction. The fraction of motion pixels in each frame, which scales with the amount of tail movement, was low-pass–filtered with a 10-ms time constant to obtain the instantaneous swim strength (ISS). This low-pass filter simulates the inertial effects experienced by larval fish in water. The ISS was streamed in real time using Open Sound Control protocol to custom software written in Processing 2.2.1 (https://processing.org/). This software generated the visual stimulus, executed the experimental protocol, and generated transistor-transistor logic (TTL) signals to synchronize two-photon imaging or electrophysiology data acquisition with visual stimulus presentation.

ISS for the electrophysiology preparation was estimated from fictive swims recorded unilaterally from the ventral root (Fig. 7A). Analog output from the recording amplifier was digitized at 12 kHz in 10-ms chunks (PCIe-6361, National Instruments) and acquired using a Bonsai workflow. Each 10-ms chunk was band-pass–filtered between 0.2 and 5 kHz. The SD of each chunk was calculated, and the offset induced by recording noise was subtracted. This signal was low-pass–filtered at 10 Hz and thresholded manually to obtain an estimate of the ISS, which was streamed to the experiment control software.

The ISS was scaled individually for each fish to obtain a realistic estimate of swim velocity. One to three trials of optic flow at 10 mm/s lasting 10 to 15 s were presented before the start of each experiment in the open-loop configuration. A scaling factor, *s*, was calculated from these trials such that the ISS when scaled resulted in an average swim bout velocity of 12 to 15 mm/s. This process is described by the following equation

$$vswim_n = s \times g \times ISS_n$$

where *n* is the frame count, *vswim* is the instantaneous velocity of the fish in the closed-loop environment, *s* is the scaling factor set individually for each fish, *g* is the gain of the closed-loop feedback, set at 1.0 for all experiments, and *ISS* is the instantaneous swim strength.

Visual stimulus

Custom software written in Processing 2.2.1 was used to control the experimental protocol as well as to generate and update the visual stimulus at 120 Hz. The visual stimulus consisted of square-wave

grating with a spatial period of 10 mm presented 5 mm beneath the fish. The grating velocity was a combination of both the stimulus velocity and the scaled ISS, as per the following equation

$$vgrating_n = vflow_n - vswim_n$$

where $vgrating_n$, $vflow_n$, and $vswim_n$ are the instantaneous velocities at frame n of the grating stimulus, externally imposed optic flow and the fish, respectively.

In the calcium imaging setup, visual stimulus was projected on a 60-mm-diameter diffusive paper screen placed 5 mm below the fish. The projector was custom-built around a 5-inch (127-mm) liquid crystal display (LCD) panel (Adafruit) removed from its housing. The LCD was illuminated from behind with a collimated 617-nm LED (Luxeonstar) and was imaged onto the projection screen. A custom-made driver was used to power the LED antiphase to the line scans of the fast x-galvo during two-photon imaging. This eliminated the possibility of bleedthrough of light from the visual stimulus into the calcium imaging channel. In addition to this, a long-pass filter (575lp, Chroma) was placed in the projection light path to prevent harmful levels of light from reaching the photomultiplier tube (PMT). The final pixel size on the projection screen was 0.32 mm. A 5 mm–by–5 mm window was cut out in the projection screen to facilitate video recording of tail movements from below (Fig. 2A). Visual stimulus for the electrophysiology experiments was presented directly on an LCD screen positioned beneath the fish.

Experimental protocols

Optic flow stimuli

Optic flow stimuli were presented in 2-s-long pulses, separated by an interval of 5 s with stationary gratings. Each trial consisted of multiple pulses of optic flow stimuli and trials began with 5 s of stationary gratings followed by a 2-s pulse. During this 2-s pulse, the gratings moved continuously for the stimuli at 1 cm/s. In case of the probe stimuli, the gratings moved with an average velocity of either +0.064 (positive probe) or −0.064 (negative probe) cm/s, corresponding to either (i) four 1-pixel steps over a 2-s period in Figs. 2 to 6 or (ii) one to three steps in Figs. 1 and 7. These stimuli are represented in the figures by their average velocity. In experiments involving more than one trial, an ITI of 30 s was introduced between trials when stationary gratings were presented. Imaging began at the onset of every trial and was stopped 6 s after the trial ended, resulting in a 24-s gap in two-photon acquisition between trials. Behavior data were acquired continuously throughout the whole protocol.

Two-photon calcium imaging

Imaging was performed on a custom two-photon microscope controlled using ScanImage 3.8 (*45*). A Ti-Sapphire laser (Chameleon Ultra II, Coherent) tuned to 920 nm was used to excite GCaMP6s. The laser was focussed at the sample using a 20× 1.0–numerical aperture (NA) objective lens (XLUMPLFLN20XW, Olympus), downstream of 50- and 300-mm focal length scan and tube lenses (AC-300-050B and AC-508-300-B, Thorlabs). Scanning was achieved using 3-mm aperture scan mirrors (6215H, Cambridge Technology). Fluorescence emission from GCaMP was band-pass–filtered (FF01-520/70, Semrock) and detected with a GaAsP PMT (H7422PA-40, Hamamatsu). Output from the PMT was amplified using a preamplifier (SR570, Stanford Research Systems) and acquired using the same data acquisition card used to drive the scan mirrors (PCI-6110, National Instruments). Data acquisition from the microscope was triggered by a TTL pulse generated at the beginning of each trial by an Arduino connected to a separate computer running the behavior protocol. A continuous time series of two-photon images was acquired for every trial of the experimental protocol. Multitrial protocols had an ITI of 30 s. Imaging was discontinued for 24 s of the 30-s interval.

PC calcium imaging

Head-restrained *Tg(aldoca:GCaMP6s);nacre*$^{-/-}$ larvae were used to image PC calcium activity. A single 512 × 128 pixel field of view with 0.53-μm pixel size, centered around the PC layer, was scanned using a pixel dwell time of either 1.6 μs (Fig. 7) or 3.2 μs (all other experiments), resulting in frame rates of either 7.8 or 3.9 Hz, respectively. Laser power measured at the sample plane was 10 to 15 mW for 3.2-μs pixel dwell time and 20 to 30 mW when the pixel time was set at 1.6 μs.

GC calcium imaging

Head-restrained *Tg(neurod:GCaMP6f);nacre*$^{-/-}$ larvae were used to image GC calcium activity. Six planes separated by 10 μm were imaged in every fish, starting from the dorsal side of the GC layer. The two-trial behavior protocol was carried out serially for each imaging plane. Because galvo scanning was used, we scanned a single hemisphere of the GC layer, alternating between left and right sides across fish, to achieve sufficient frame rate for GCaMP6f while still densely sampling the cell population. A 256 × 128 pixel field of view with 0.53-μm pixel size was scanned with a pixel time of 3.2 μs, resulting in a frame rate of 7.8 Hz. Laser power used for GC imaging was in the range of 15 to 20 mW at the sample plane. After acquisition, a two-frame temporal averaging was used to improve signal to noise ratio to aid subsequent analysis.

Two-photon laser ablations

Tg(aldoca:GCaMP6s);nacre$^{-/-}$ larvae were prepared for cerebellum ablations using the same protocol as used for the calcium imaging experiments. Ten planes within the PC layer, separated by 4 μm, were serially scanned with a pixel dwell time of 1.6 μs. Ablations were confined to the PC layer using visual aid from GCaMP fluorescence. The laser was tuned to 920 nm with a power of ~230 mW at the sample plane. Each plane was scanned 10 times before moving to the next. This led to effective plasma mediated lesioning of the whole cerebellar region being scanned. Lesions were confirmed visually by an immediate increase in fluorescence intensity due to uncontrolled influx of calcium into the cytosol, followed by blebbing and disintegration of cells. Fish were allowed to recover for 1 hour after lesion before initiating the behavior protocol. The cerebellum was scanned while the behavior protocol was carried out, with laser power and scan settings identical to those used for calcium imaging in nonlesioned fish to maintain experimental conditions.

Electrophysiology

Six- to 7-dpf zebrafish larvae were first anesthetized in 0.01% MS-222 and transferred to a recording chamber. Two pieces of fine tungsten wire (California Fine Wire) were used to pin the larvae through the notochord onto a Sylgard (Dow Corning) slab in the recording chamber. A third pin was used to orient the head dorsal side up (Fig. 7A). The MS-222 was then replaced by external solution (composition: 134 mM NaCl, 2.9 mM KCl, 1.2 mM $MgCl_2$, 10 mM Hepes, 10 mM glucose, 2.1 mM $CaCl_2$, and 0.01 mM d-tubocurarine; pH 7.8; 290 mosmol), and the skin covering the brain and along the tail was carefully removed using forceps (Fine Science Tools). The preparation was then taken to a rig apparatus.

Patch pipettes for loose-patch recordings were made using thick-walled borosilicate capillaries [1.5-mm outer diameter (OD) and 0.86-mm inner diameter (ID), Warner Instruments] and pulled to 1- to 1.5-μm tip diameter using a Flaming Brown P-97 pipette puller (Sutter Instruments), such that their resistance when backfilled with external solution was approximately 7 to 10 megaohms. Similarly, suction recording pipettes for fictive motor recordings were made using thin-walled borosilicate capillaries (1.5-mm OD and 1.1-mm ID, Sutter Instruments) and pulled to ~5-μm tip diameter, such that their resistance when backfilled with external solution was ~0.7 to 1.5 megaohms.

First, ventral root recordings to monitor fictive swimming were obtained by guiding the pipette to a myotomal boundary (~15th to 20th somite) and applying mild suction. Once a successful recording was obtained, the focus was shifted to the cerebellum, and loose-patch recordings from Purkinje neurons were obtained. The pipettes were guided visually using a 60× 1.0-NA water immersion objective of a compound microscope (Ni-E, Nikon) and a motorized micromanipulator (PatchStar, Scientifica). Once both recordings were obtained, the condenser of the microscope was gently moved to allow the introduction of a 5-inch (127-mm) LCD screen (Adafruit) to present visual stimuli.

Visual stimulus presentation and electrophysiological recordings were triggered simultaneously and acquired using a Multiclamp 700B amplifier, Digidata 1440A digitizer, and pCLAMP software (Molecular Devices). The data were low-pass–filtered at 2 kHz using a Bessel filter and sampled at 50 kHz at a gain between 10 and 2000, adjusted depending on the quality of each recording. The ventral root recordings were parallely acquired, and real-time analysis was performed to provide closed-loop optomotor feedback as described above.

Calcium trace extraction

Calcium traces were extracted from individual PC somata using a semi-automated processing pipeline written in Python. The images were corrected for translation along the *xy* plane using phase correlation with the registration module in scikit-image (*46*). For multitrial experiments, all frames were aligned to the first frame of the first trial, and the accuracy of the registration was verified manually for every trial.

Regions of interest (ROIs) marking individual cells were drawn using a semiautomated process. For PCs, the location of individual cells was identified manually using a graphical user interface (GUI). A three-layer neural network trained using a subset of data from these experiments was used to mark cell boundaries, guided by the manually identified coordinates. For GCs, coordinates were identified using a 2D local minimum intensity function, followed by manual pruning. Cell boundaries were then drawn by detecting bright cytoplasmic GCaMP fluorescence using a threshold function applied radially around the coordinates identified. Overlapping pixels assigned to more than one ROI were excluded from any of the assigned ROIs to avoid signal contamination from neighboring cells.

Pixels within the ROI were averaged to obtain fluorescence intensity of each cell for a given frame. The fold change in fluorescence intensity over baseline (dF/F) was calculated with the baseline estimated as the 10th percentile of the fluorescence intensity for each cell over time using the formula: $dF/F = (F - F_b)/(F_b)$, where F is the fluorescence intensity for a given frame and F_b is the baseline fluorescence estimated as described. In case of multitrial experiments, the baseline was updated once for each trial. For the continuous 700-s-long recordings shown in Fig. 7, baseline was calculated for each frame as the 10th percentile of a 1-min window around that frame. Two-frame temporal averaging was used for all analyses in case of GCs to improve signal-to-noise ratio. A two-frame temporal averaging was performed for the regression analysis for PCs.

Data processing and analysis

Data processing and analysis were done primarily using Python (python.org). Event detection for the electrophysiology recordings was done using MATLAB (MathWorks).

Behavior data processing

Swim velocity data and time stamps saved from the experiment control software at ~120 Hz were used for estimating latency. A simple threshold was sufficient to detect the beginning and end of swim bouts as the signal-to-noise ratios were sufficiently high.

Estimating latency modulation

Latency modulation around the probe stimulus was estimated by determining the fold change in response latency relative to baseline latency (Fig. 1B and fig. S4). The baseline was determined as the mean latency observed across five pulses of forward optic flow at 1 cm/s before the probe pulse. This normalization was necessary as slow drifts in latency developed over the duration of the experiment. Traces were selected if there were at least three swim bouts on either side of the probe stimulus within a window of five forward optic flow stimuli. A minimum of three such traces were required per fish to obtain an average latency modulation trace for that fish. Seventeen of the 27 nonlesioned fish (Fig. 1C) and 11 of the 11 cerebellum lesioned fish (Fig. 1D) passed these exclusion criteria. For the experiment in fig. S4, latency modulation was estimated relative to the median latency of all trials. Trials were chosen if the response rate of fish was above 50%. A minimum of three such trials were required per fish to obtain an average latency modulation trace for that fish. Twelve of the 15 fish passed these criteria and were used for the analysis.

Spike detection and analysis

Spikes were identified as events that showed large fluctuations relative to a 25-ms rolling window baseline, and the peak times and amplitudes were extracted. Small-amplitude events were classified as SSs, and large-amplitude events were classified as CF inputs (*22*). Once identified and sorted, recordings were triggered to the start of optic flow. Mean firing rates were estimated by convolving peri-event time histograms of 20-ms binwidth with a 200-ms Gaussian kernel. Analysis was done using custom scripts written in Python. CF/SS event detection was done in MATLAB (https://github.com/wagenadl/mbl-nsb-toolbox).

Statistics

All statistical tests were performed in Python using SciPy (*47*), statsmodels (*48*), and scikit-posthocs (*49*). The statistical tests used and their results are mentioned in the figure legends. In cases where linear mixed-effects models are used, both random intercept and random slopes were included to test whether the population showed a nonzero slope. Fitting was done using the formula interface in the statsmodels package.

Supplementary Materials

This PDF file includes:

Figs. S1 to S7
Table S1

REFERENCES AND NOTES

1. K. Friston, The free-energy principle: A unified brain theory? *Nat. Rev. Neurosci.* **11**, 127–138 (2010).
2. G. B. Keller, T. D. Mrsic-Flogel, Predictive processing: A canonical cortical computation. *Neuron* **100**, 424–435 (2018).
3. T. Kawashima, M. F. Zwart, C.-T. Yang, B. D. Mensh, M. B. Ahrens, The serotonergic system tracks the outcomes of actions to mediate short-term motor learning. *Cell* **167**, 933–946.e20 (2016).
4. A. Kennedy, G. Wayne, P. Kaifosh, K. Alviña, L. F. Abbott, N. B. Sawtell, A temporal basis for predicting the sensory consequences of motor commands in an electric fish. *Nat. Neurosci.* **17**, 416–422 (2014).

5. M. Leinweber, D. R. Ward, J. M. Sobczak, A. Attinger, G. B. Keller, A sensorimotor circuit in mouse cortex for visual flow predictions. *Neuron* **95**, 1420–1432.e5 (2017).
6. W. Schultz, P. Dayan, P. R. Montague, A neural substrate of prediction and reward. *Science* **275**, 1593–1599 (1997).
7. A. Fiser, D. Mahringer, H. K. Oyibo, A. V. Petersen, M. Leinweber, G. B. Keller, Experience-dependent spatial expectations in mouse visual cortex. *Nat. Neurosci.* **19**, 1658–1664 (2016).
8. A. R. Garner, G. B. Keller, A cortical circuit for audio-visual predictions. *Nat. Neurosci.* **25**, 98–105 (2022).
9. M. Torigoe, T. Islam, H. Kakinuma, C. C. A. Fung, T. Isomura, H. Shimazaki, T. Aoki, T. Fukai, H. Okamoto, Zebrafish capable of generating future state prediction error show improved active avoidance behavior in virtual reality. *Nat. Commun.* **12**, 5712 (2021).
10. J. P. Hamm, Y. Shymkiv, S. Han, W. Yang, R. Yuste, Cortical ensembles selective for context. *Proc. Natl. Acad. Sci. U. S. A.* **118**, e2026179118 (2021).
11. S. Han, F. Helmchen, Behavior-relevant top-down cross-modal predictions in mouse neocortex. bioRxiv 535389 [Preprint]. 2023. https://doi.org/10.1101/2023.04.03.535389.
12. S. Narayanan, V. Thirumalai, Contributions of the cerebellum for predictive and instructional control of movement. *Curr. Opin. Physio.* **8**, 146–151 (2019).
13. C. Hull, Prediction signals in the cerebellum: Beyond supervised motor learning. *eLife* **9**, e54073 (2020).
14. W. Schultz, Dopamine signals for reward value and risk: Basic and recent data. *Behav. Brain Funct.* **6**, 24 (2010).
15. D. M. Wolpert, R. C. Miall, M. Kawato, Internal models in the cerebellum. *Trends Cogn. Sci.* **2**, 338–347 (1998).
16. R. Shadmehr, M. A. Smith, J. W. Krakauer, Error correction, sensory prediction, and adaptation in motor control. *Annu. Rev. Neurosci.* **33**, 89–108 (2010).
17. M. J. Wagner, T. H. Kim, J. Savall, M. J. Schnitzer, L. Luo, Cerebellar granule cells encode the expectation of reward. *Nature* **544**, 96–100 (2017).
18. D. Kostadinov, M. Beau, M. Blanco-Pozo, M. Häusser, Predictive and reactive reward signals conveyed by climbing fiber inputs to cerebellar Purkinje cells. *Nat. Neurosci.* **22**, 950–962 (2019).
19. W. Heffley, C. Hull, Classical conditioning drives learned reward prediction signals in climbing fibers across the lateral cerebellum. *eLife* **8**, e46764 (2019).
20. C. C. Bell, V. Han, N. B. Sawtell, Cerebellum-like structures and their implications for cerebellar function. *Annu. Rev. Neurosci.* **31**, 1–24 (2008).
21. Y.-K. Bae, S. Kani, T. Shimizu, K. Tanabe, H. Nojima, Y. Kimura, S. Higashijima, M. Hibi, Anatomy of zebrafish cerebellum and screen for mutations affecting its development. *Dev. Biol.* **330**, 406–426 (2009).
22. M. Sengupta, V. Thirumalai, AMPA receptor mediated synaptic excitation drives state-dependent bursting in Purkinje neurons of zebrafish larvae. *eLife* **4**, e09158 (2015).
23. T. C. Harmon, U. Magaram, D. L. McLean, I. M. Raman, Distinct responses of Purkinje neurons and roles of simple spikes during associative motor learning in larval zebrafish. *eLife* **6**, e22537 (2017).
24. Q. Lin, J. Manley, M. Helmreich, F. Schlumm, J. M. Li, D. N. Robson, F. Engert, A. Schier, T. Nöbauer, A. Vaziri, Cerebellar neurodynamics predict decision timing and outcome on the single-trial level. *Cell* **180**, 536–551.e17 (2020).
25. S. C. F. Neuhauss, O. Biehlmaier, M. W. Seeliger, T. Das, K. Kohler, W. A. Harris, H. Baier, Genetic disorders of vision revealed by a behavioral screen of 400 essential loci in zebrafish. *J. Neurosci.* **19**, 8603–8615 (1999).
26. M. B. Orger, M. C. Smear, S. M. Anstis, H. Baier, Perception of Fourier and non-Fourier motion by larval zebrafish. *Nat. Neurosci.* **3**, 1128–1133 (2000).
27. E. A. Naumann, J. E. Fitzgerald, T. W. Dunn, J. Rihel, H. Sompolinsky, F. Engert, From whole-brain data to functional circuit models: The zebrafish optomotor response. *Cell* **167**, 947–960.e20 (2016).
28. R. Portugues, F. Engert, Adaptive locomotor behavior in larval zebrafish. *Front. Syst. Neurosci.* **5**, 72 (2011).
29. A. Bahl, F. Engert, Neural circuits for evidence accumulation and decision making in larval zebrafish. *Nat. Neurosci.* **23**, 94–102 (2020).
30. R. Portugues, M. Haesemeyer, M. L. Blum, F. Engert, Whole-field visual motion drives swimming in larval zebrafish via a stochastic process. *J. Exp. Biol.* **218**, 1433–1443 (2015).
31. K. E. Severi, R. Portugues, J. C. Marques, D. M. O'Malley, M. B. Orger, F. Engert, Neural control and modulation of swimming speed in the larval zebrafish. *Neuron* **83**, 692–707 (2014).
32. Y. Mu, D. V. Bennett, M. Rubinov, S. Narayan, C.-T. Yang, M. Tanimoto, B. D. Mensh, L. L. Looger, M. B. Ahrens, Glia accumulate evidence that actions are futile and suppress unsuccessful behavior. *Cell* **178**, 27–43.e19 (2019).
33. M. Sengupta, thesis, Tata Institute of Fundamental Research, Mumbai (2015).
34. A. Varma, S. Udupa, M. Sengupta, P. K. Ghosh, V. Thirumalai, A machine-learning tool to identify bistable states from calcium imaging data. bioRxiv 10.515941 [Preprint]. 2022. https://doi.org/10.1101/2022.11.10.515941.
35. L. D. Knogler, A. M. Kist, R. Portugues, Motor context dominates output from purkinje cell functional regions during reflexive visuomotor behaviours. *eLife* **8**, e42138 (2019).
36. R. Felix, D. A. Markov, S. L. Renninger, R. Tomás, A. Laborde, M. R. Carey, M. B. Orger, R. Portugues, Structural and functional organization of visual responses in the inferior olive of larval zebrafish. bioRxiv 470378 [Preprint]. 2021. https://doi.org/10.1101/2021.11.29.470378.
37. A. Miri, K. Daie, R. D. Burdine, E. Aksay, D. W. Tank, Regression-based identification of behavior-encoding neurons during large-scale optical imaging of neural activity at cellular resolution. *J. Neurophysiol.* **105**, 964–980 (2011).
38. A. Kramer, Y. Wu, H. Baier, F. Kubo, Neuronal architecture of a visual center that processes optic flow. *Neuron* **103**, 118–132.e7 (2019).
39. L. D. Knogler, D. A. Markov, E. I. Dragomir, V. Štih, R. Portugues, Sensorimotor representations in cerebellar granule cells in larval zebrafish are dense, spatially organized, and non-temporally patterned. *Curr. Biol.* **27**, 1288–1302 (2017).
40. O. Prat, L. Petrucco, V. Štih, R. Portugues, Comparing the representation of a simple visual stimulus across the cerebellar network. bioRxiv 507660 [Preprint]. 2022. https://doi.org/10.1101/2022.09.12.507660.
41. A. Giovannucci, A. Badura, B. Deverett, F. Najafi, T. D. Pereira, Z. Gao, I. Ozden, A. D. Kloth, E. Pnevmatikakis, L. Paninski, C. I. De Zeeuw, J. F. Medina, S. S.-H. Wang, Cerebellar granule cells acquire a widespread predictive feedback signal during motor learning. *Nat. Neurosci.* **20**, 727–734 (2017).
42. P. Rupprecht, A. Prendergast, C. Wyart, R. W. Friedrich, Remote z-scanning with a macroscopic voice coil motor for fast 3D multiphoton laser scanning microscopy. *Biomed. Opt. Express.* **7**, 1656–1671 (2016).
43. G. Lopes, N. Bonacchi, J. Frazão, J. P. Neto, B. V. Atallah, S. Soares, L. Moreira, S. Matias, P. M. Itskov, P. A. Correia, R. E. Medina, L. Calcaterra, E. Dreosti, J. J. Paton, A. R. Kampff, Bonsai: An event-based framework for processing and controlling data streams. *Front. Neuroinform.* **9**, 7 (2015).
44. M. B. Ahrens, J. M. Li, M. B. Orger, D. N. Robson, A. F. Schier, F. Engert, R. Portugues, Brain-wide neuronal dynamics during motor adaptation in zebrafish. *Nature* **485**, 471–477 (2012).
45. T. A. Pologruto, B. L. Sabatini, K. Svoboda, ScanImage: Flexible software for operating laser scanning microscopes. *Biomed. Eng. Online* **2**, 13 (2003).
46. S. van der Walt, J. L. Schönberger, J. Nunez-Iglesias, F. Boulogne, J. D. Warner, N. Yager, E. Gouillart, T. Yu; the scikit-image contributors, Image processing in Python. *PeerJ.* **2**, e453 (2014).
47. P. Virtanen, R. Gommers, T. E. Oliphant, M. Haberland, T. Reddy, D. Cournapeau, E. Burovski, P. Peterson, W. Weckesser, J. Bright, S. J. van der Walt, M. Brett, J. Wilson, K. J. Millman, N. Mayorov, A. R. J. Nelson, E. Jones, R. Kern, E. Larson, C. J. Carey, İ. Polat, Y. Feng, E. W. Moore, J. V. Plas, D. Laxalde, J. Perktold, R. Cimrman, I. Henriksen, E. A. Quintero, C. R. Harris, A. M. Archibald, A. H. Ribeiro, F. Pedregosa, P. van Mulbregt; SciPy 1.0 Contributors, A. Vijaykumar, A. P. Bardelli, A. Rothberg, A. Hilboll, A. Kloeckner, A. Scopatz, A. Lee, A. Rokem, C. N. Woods, C. Fulton, C. Masson, C. Häggström, C. Fitzgerald, D. A. Nicholson, D. R. Hagen, D. V. Pasechnik, E. Olivetti, E. Martin, E. Wieser, F. Silva, F. Lenders, F. Wilhelm, G. Young, G. A. Price, G.-L. Ingold, G. E. Allen, G. R. Lee, H. Audren, I. Probst, J. P. Dietrich, J. Silterra, J. T. Webber, J. Slavič, J. Nothman, J. Buchner, J. Kulick, J. L. Schönberger, J. V. de Miranda Cardoso, J. Reimer, J. Harrington, J. L. C. Rodríguez, J. Nunez-Iglesias, J. Kuczynski, K. Tritz, M. Thoma, M. Newville, M. Kümmerer, M. Bolingbroke, M. Tartre, M. Pak, N. J. Smith, N. Nowaczyk, N. Shebanov, O. Pavlyk, P. A. Brodtkorb, P. Lee, R. T. M. Gibbon, R. Feldbauer, S. Lewis, S. Tygier, S. Sievert, S. Vigna, S. Peterson, S. More, T. Pudlik, T. Oshima, T. J. Pingel, T. P. Robitaille, T. Spura, T. R. Jones, T. Cera, T. Leslie, T. Zito, T. Krauss, U. Upadhyay, Y. O. Halchenko, Y. Vázquez-Baeza, SciPy 1.0: Fundamental algorithms for scientific computing in Python. *Nat. Methods* **17**, 261–272 (2020).
48. S. Seabold, J. Perktold, "Statsmodels: Econometric and statistical modeling with Python," paper presented at the Proceedings of the 9th Python in Science Conference (SciPy 2010), Austin, TX, 28 June 28 to 3 July 2010.
49. M. A. Terpilowski, Scikit-posthocs: Pairwise multiple comparison tests in Python. *J. Open Source Softw.* **4**, 1169 (2019).

Acknowledgments: We would like to thank M. Hibi for providing the *Tg(aldoca:GCaMP6s);nacre*$^{-/-}$ fish line and C. Wyart and A. Prendergast for the *Tg(neurod:GCaMP6f);nacre*$^{-/-}$ fish line. Further thanks are also due to P. T. Jagadeesh for the maintenance of our fish lines and to L. Robra, M. Modi, and E. George for providing advice and assistance. In addition, we would like to thank the Central Imaging and Flow Facility at NCBS for support. **Funding:** This work was supported by Wellcome Trust-DBT India Alliance Intermediate fellowship, 500040/Z/09/Z (V.T.); Wellcome Trust-DBT India Alliance Senior fellowship, IA/S/17/2/503297 (V.T.); Department of Biotechnology, BT/PR4983/MED/30/790/2012 (V.T.); Science and Engineering Research Board, EMR/2015/000595 (V.T.); Department of Atomic Energy (V.T.); and NCBS-TIFR graduate student fellowship (S.N. and A.V.).
Author contributions: Conceptualization: S.N. and V.T. Methodology: S.N. and A.V. Investigation: S.N. and A.V. Visualization: S.N. Supervision: S.N., A.V., and V.T. Writing—original draft: S.N. and V.T. Writing—review and editing: S.N., A.V., and V.T. **Competing interests:** The authors declare that they have no competing interests. **Data and materials availability:** All data needed to evaluate the conclusions in the paper are present in the paper and/or the Supplementary Materials. We have made data and analysis scripts available for the reviewers and all readers on Zenodo. A zip folder containing data and code can be downloaded from the url: https://doi.org/10.5281/zenodo.8396667. This folder contains a document with instructions to generate figures in the paper from the included data.

Submitted 9 May 2023
Accepted 1 December 2023
Published 3 January 2024
10.1126/sciadv.adi6470